Highly Active and Stable Large Mo-doped Pt-Ni Octahedral Catalysts for ORR: Synthesis, Post-treatments and Electrochemical Performance and Stability

Shlomi Polani,[*a†] Katherine E. MacArthur,[b†] Jiaqi Kang,[a] Malte Klingenhof,[a] Xingli Wang,[a]

Tim Möller,[a] Raffaele Amitrano,[a] Raphaël Chattot,[c] Marc Heggen,[*b] Rafal E. Dunin-Borkowski,[b] and Peter Strasser[*a]

[a]Electrochemical Energy, Catalysis and Material Science Laboratory, Department of Chemistry, Technical University Berlin, 10623 Berlin, Germany

[b]Ernst Ruska-Centre for Microscopy and Spectroscopy with Electrons and Peter Grünberg Institute, Forschungszentrum Jülich GmbH, 52425 Jülich, Germany

[c]ICGM, Univ. Montpellier, CNRS, ENSCM, 34095 Montpellier cedex 5, France

†These authors contributed equally to the article.

Keywords: Oxygen reduction, Platinum–nickel alloy, Mo-dopant, Durability, Synthesis, LaMer model

Abstract

Over the past decade, advances in the colloidal syntheses of octahedral shaped Pt-Ni alloy nanocatalysts for use in Fuel Cell cathodes have raised our atomic-scale control of particle morphology and surface composition, which, in turn, helped raise their catalytic activity far above that of benchmark Pt catalysts. Future fuel cell deployment in heavy-duty vehicles caused the scientific priorities to shift from alloy particle activity to stability. Larger particles generally offer enhanced thermodynamic stability, yet synthetic approaches towards larger octahedral Pt-Ni alloy nanoparticles have remained elusive. In this study, we show how a simple manipulation of solvothermal synthesis reaction kinetics involving depressurization of the gas phase at different stages of the reaction allows tuning the size of the resulting octahedral nanocatalysts to previously unachieved scales. We then link the underlying mechanism of our approach to the classical "LaMer" model of nucleation and growth. We focus on large, annealed Mo-doped Pt-Ni octahedra and investigate their synthesis, post-synthesis treatments, and elemental distribution using advanced electron microscopy. We evaluate the electrocatalytic ORR performance and stability and succeed to obtain a deeper understanding of the enhanced stability of a new class of relatively large, active and long-lived Mo-doped Pt-Ni octahedral catalyst for the cathode of PEMFCs.

Introduction

Climate change due to anthropogenic carbon emissions alongside concomitant fossil fuel depletion are serious immediate global challenges. To meet these challenges, the development of low-emission energy technologies such as hydrogen fuel cells for use in energy conversion and storage applications is of great importance. Proton exchange membrane fuel cells (PEMFCs) have been the focus of interest for many years.[1] The major challenge for automotive application is the development of an active, economical, and durable electrocatalyst for the oxygen reduction reaction (ORR) that occurs at the fuel cell cathode.[2] Early studies of the ORR kinetics of extended Pt surfaces have shown that it varies with crystallographic orientation and that the activity for low-index facets increases as follows (100) < (111) < (110) (in 0.1 M $HClO_4$).[3] Subsequent studies on smooth and extended low-index (in macroscopic size) bimetallic Pt-M surfaces showed volcano-shaped ORR activity plot, where alloying Pt with certain 3d transition metals or lanthanides increases intrinsic ORR activity.[4–7] These alloy surfaces are more catalytically active than pure Pt due to the formation of surface lattice strain associated with a downwardly shifted d-band center. Noteworthy, was the $Pt_3Ni(111)$ single crystal facet, which exhibited an almost 100-fold increase in intrinsic ORR activity compared to Pt nanoparticles (NPs). Later, the popular "materials-by-design" strategy,[8] which involves translating the knowledge acquired from single-crystals to nanoscale catalysts, led to a new line of Pt catalyst research focused on "small" 4−9 nm-sized, Pt-rich, shape-controlled octahedral Pt-Ni (oh-PtNi) NPs that are exclusively enclosed with PtNi(111) facets. Focus on this size range was justified by the required mass specific surface area of the particles. These 4–9 nm oh-PtNi have indeed showed enhanced electrocatalytic ORR activities in idealized Rotating Disk Electrode (RDE) tests in recent years.[9]

The reduction of Pt(II) and Ni(II) acetylacetonate compounds by dimethylformamide (DMF) as the solvent and the reducing agent is a common synthesis procedure to produce oh-PtNi NPs. The syntheses are usually performed in a sealed vessel and the reaction temperature is typically above the boiling points of DMF and acetylacetonate ligand (153 and 140 °C, respectively).[10–13] The moderate 25-at% Ni content and thus Pt content in the resulting octahedral Pt_3Ni NPs, as well as the finding that DMF is a weak reducing

agent,[10,12] cast doubt on the ability of DMF to quantitatively reduce $Ni(acac)_2$ from Ni^{II} to Ni^0 under these conditions. Moreover, Pt-rich oh-PtNi NPs have been synthesized using a mixture of oleylamine and oleic acid, as a solvent and capping agents, with or without tungsten hexacarbonyl as reducing and shaping agents at relatively high temperatures (above 200 °C).[14–18] But again, the sizes of the resulting catalysts are generally small, about 4–9 nm in edge length. Wu et al.[19] reported the use of benzyl alcohol (BA) to obtain 11.8 ± 1.2 nm (apex to opposite apex) oh-PtNi catalysts with a wide range of atomic Pt compositions. However, these catalysts were never studied for the ORR, rather for a model hydrogenation reaction. Nevertheless, oh-PtNi catalysts are unstable during electrochemical cycling due to leaching of Ni, resulting in the loss of the ideal (111) facets that are thought to give them their outstanding activity. Doping with a third metal further improves the performance of oh-PtNi by optimizing the local oxygen binding energies and stabilizing Ni in the Pt lattice.[20,21] Doping Mo,[22] Rh[23] or Ga,[24] into oh-PtNi catalysts resulted in increased activity and stability.

Today, there is a consensus that the intrinsic, surface area-normalized, specific ORR activity is a key controlling parameter for the design of active catalysts made up of shaped oh-PtNi NPs. The specific ORR activity depends on the fraction and surface atomic composition of exposed PtNi(111) facets. Currently, the specific activity (SA) for the typical oh-PtNi NPs is about an order of magnitude lower than that of single-crystal $Pt_3Ni(111)$ surfaces.[25] The desired well-defined $Pt_3Ni(111)$ surfaces showed turnover frequencies of about 2800 s^{-1}, which, when translated to the NPs scale, correlates with oh-catalysts with a diameter of around 30 nm. Moreover, the durability of nanocatalysts based on a 30 nm Pt alloy is greatly improved, as deduced from studies with thin-film alloys and large NPs. Larger particles have fewer Low-coordination surface adatoms, which leads to a decrease in Pt dissolution during voltage cycling.[7,25–30] Strategies for the preparation of 30 nm-diameter (corresponds to 21 nm edge length in a regular octahedron) oh-PtNi NPs have however remained elusive to date.

In a pioneering first attempt, the LaMer growth model,[31] which postulates instantaneous nucleation followed by diffusion-controlled growth, was widely adopted by the science community, to understand the formation of nearly micrometer-sized monodisperse particles via self-assembly.[32] In instantaneous nucleation, nuclei are produced simultaneously by homogeneous nucleation and subsequently grow in a diffusion controlled regime without further nucleation events occurring. The principle of this approach to NPs formation is to separate and independently control nucleation and growth, allowing precise control of particle size distribution.

Typically, Pt-based alloy NPs with large diameters and smooth surfaces do not necessarily result in higher Pt mass activities due to their low Pt atoms utilization. Therefore, the main challenge in using large Pt-M NPs for ORR is to produce Pt-M NPs that utilizes Pt atoms on their surfaces for high performance and stability simultaneously. In bimetallic systems, surface enrichment may occur as one element binds a particular adsorbate more strongly.[33] Thermal annealing of Pt-M NPs in a reducing atmosphere is another way to fabricate the desired surface structure and stable composition profile.[34–36]

Herein we report the ability to tune the size of Mo-doped oh-PtNi catalysts (henceforth oh-PtNi(Mo)) toward previously unachieved scales approaching the desired 30nm/21nm edge length regime. We focus on the preparation of different sizes and surface compositions using a new hypothesis based on a modified LaMer model. We also investigate the relationship between the size of the NPs and their elemental distribution before and after annealing in a reducing or oxidizing atmosphere and correlate this with performance and stability.

Experimental Section

Materials

Platinum (II) acetylacetonate ($Pt(acac)_2$, ≥98%) was obtained from Acros, nickel (II) acetylacetonate ($Ni(acac)_2$, ≥98%), molybdenum hexacarbonyl ($Mo(CO)_6$, 99.9%) and Nafion solution (5% w/w) were obtained from Sigma Aldrich. Platinum on activated carbon powder, from Johnson Matthey Fuel Cells (Pt/C, 50 Ptw%). Polyvinylpyrrolidone (M. W. 10,000) and benzoic acid (99%) were obtained from Alfa Aesar. Benzyl alcohol (≥99%) was purchased from Carl-Roth, acetone and ethanol were purchased from VWR International. Carbon black (Vulcan XC-72R) was obtained from Cabot Corporation. All chemicals were used as received.

Syntheses of oh-PtNi(Mo)/C NPs

For PtNi(Mo)/C-13: $Pt(acac)_2$ (64.0 mg, 162.8 µmol, 1.00 equiv.), $Ni(acac)_2$ (200.0 mg, 778.5 µmol, 4.78 equiv. to $Pt(acac)_2$), $Mo(CO)_6$ (20.0 mg, 75.8 µmol, 0.47 equiv.), PVP (640 mg, M.W. 10,000), and benzoic acid (400 mg, 3.28 mmol) were weighed into a pressure flask vessel with a magnetic stir bar and dissolved in BA (60 mL). The flask vessel was heated from room temperature to 60 °C and kept at 60 °C for 1 hour with stirring. Then the vessel was heated to 150 °C (5 °C /min) and kept at 150 °C for 12 hours. In parallel, a suspension of Vulcan carbon (75 mg) in BA (10 mL) was prepared in a glass vessel by stirring overnight.

For PtNi(Mo)-5: The pressure was released after 2 h (from 0.5 bar_g to 0 $bar_{(g)}$), and the reaction was kept at 150 °C for another 10 h.

For PtNi(Mo)-17: The pressure was released after 4 h (from 0.6 bar_g to 0 $bar_{(g)}$), and the reaction was kept at 150 °C for another 8 h.

For PtNi-13: We have used the same conditions of PtNi(Mo)-17 but, without $Mo(CO)_6$ precursors and released the pressure in the growth stage.

After a total of 12 hours, we allowed the reaction solutions to cool to room temperature, added the Vulcan carbon solutions, and stirred overnight. The products were precipitated by centrifugation and washed three times with a mixture of ethanol and acetone.

Morphological, structural, and elemental characterization

Powder X-ray diffraction (XRD) were acquired with a D8 Advance-Diffractometer (Bruker) equipped with a Lynx Eye Detector and a KFL Cu 2K X-ray tube. The measurements were performed with a step size of 0.04°, in a 2θ range between 20 and 85°.

To extract the lattice parameter and crystallite size of the different phases composing the samples, we performed Rietveld Refinements of the XRD patterns. One, two or three Fm3m phase structures of Pt_xNi_{1-x} metal were implemented to describe at best the patterns using Fullprof software. Thomson-Cox-Hastings profile function was adopted, and the background of patterns was described by an interpolated set of points with refinable intensities.

An Inductively coupled plasma optical emission spectrometry (ICP-OES, Varian 715-ES-ICP analysis system) was used for compositional analysis. Four standard solutions of each element were prepared with concentrations of 1, 7, 12 and 20 mg/L. Approximately 5 mg of the samples were dissolved in a mixture of 2 mL H_2SO_4, 2 mL HNO_3, and 6 mL HCl. Using a microwave digestion system, the solutions were heated

to 180 °C for 10 min and held at this temperature for 20 min. After cooling to room temperature, the solutions were filtered and diluted with ultrapure water (Millipore, 18 MΩ) to achieve concentrations between 1-20 mg/L. A specific wavelength of each element was used to analyze the concentration. The concentrations of platinum, nickel and molybdenum were measured at 265.945 nm, at 231.604 nm and 268.414 nm, respectively.

In-situ high-temperature XRD (HT-XRD) measurements were performed in a parallel beam geometry using a D8 Advance-Diffractometer (Bruker) equipped with a Lynx Eye Detector (PSD) and a KFL Cu 2K X-ray tube. An external radiation heating chamber (MRI Physikalische Geraete GmbH, Germany) with an AlCr foil as heater, an Al_2O_3 crucible as sample holder and a thermocouple was positioned on the goniometer of the diffractometer. The chamber was heated to 350 ^oC under hydrogen/argon (4% H_2 in Ar) atmosphere with a flow rate of 40 mL/min. The Cu-Ka tube was operated at a voltage of 40 kV and a current of 40 mA. For sample preparation, the Al_2O_3 crucible was filled (20-30 mg) with PtNi(Mo)/C powders. The crucible was then flattened to a smooth surface and mounted on the XRD. The temperature-time protocol began with an initial XRD scan at 30 ^oC and was then heated at 0.167 ^oC/s to 350 ^oC. After holding for 30 min and a scan performed during 56 min, the temperature was cooled to 30 ^oC at the same rate. The heating protocol is shown in Figure S1. Measurements were carried out at a step size of 0.06 (8 s per step), a fix divergence slit of 1.5 mm, a PSD iris anti-scattering slit of 13, in a 2θ-Range between 30 and 55° at 350 ^oC, in a 2θ-Range between 30 and 80° at 30 ^oC.

Transmission electron microscopy (TEM) images were obtained using a FEI Tecnai G2 20 S-TWIN operating at 200 kV accelerating voltage with a resolution limit of 0.24 nm and a LaB6 cathode. For sample preparation, particles were dispersed in ethanol with ultrasonication for 5 min, drop casted onto a Cu grid (400 mesh) and air dried.

ADF-STEM-EDS investigations were carried out using a FEI Titan-80-200 (ChemiSTEM) scanning transmission electron microscope equipped with quadrant Super-X energy dispersive X-ray spectrometer (EDS) detector with a nominal 0.7 srad solid angle and operating at an accelerating voltage of 80kV. The microscope was operated at spot size 6, gun lens 6, yielding a probe with diameter of 0.1 nm and current of ~60 pA. Sample preparation as above using de-ionized water for the solvent.

Electrochemical Characterization

We carried out the electrochemical characterization using a conventional three-electrode cell with a Pt wire as counter electrode, glassy carbon (GC), with a diameter Ø=5 mm (area: 0.196 cm^2) as working electrode and a reversible hydrogen electrode (RHE) as reference electrode were used. The working electrode was lowered into the electrolyte under potential control at 0.05 V_{RHE}. The reference electrode was calibrated regularly with a polycrystalline Pt-RDE under H_2 sparging. All potentials in this work are referred to RHE. For electrochemical measurements, 0.1 M $HClO_4$ electrolyte was used (diluted from 70% conc. $HClO_4$, 99.999% trace metal bases, Sigma Aldrich with milli-Q water). All measurements were performed using a BioLogics Science Instruments potentiostat. To avoid the effects of CO-stripping on the catalyst performance, two working electrodes were used to obtain CO-stripping based ECSA before and after the accelerated stress test (AST).[37] Scheme S1, shows the flowchart of the different steps applied to two identical working electrodes.

To prepare the ink for the measurements, a certain amount of catalyst (approximately 5-6 mg) was added to a solution of 3.98 mL ultrapure water, 1 mL isopropanol, and 10 µL of a 5 wt% Nafion ionomer solution. Subsequent, the suspension was sonicated with an ultrasonic horn sonicator (Branson Sonifier 150) for 30 min while immersed in an ice bath. The ink was used the same day. 10 µl of the ink was dropped onto a rotating GC disk working electrode with a pipette. The films were dried in an oven at 60 °C.

Electrode preparation. The GC electrodes were polished with an alumina polish of 1.0 µm particle size on a nylon film for 3 min and then with an alumina polish of 0.05 µm particle size on a MicroCloth film for 3 min (Buehler Alpha). Subsequently, the electrodes were sonicated in ultrapure water, isopropanol and ultrapure water for 5 min each to obtain a clean surface.

H_{upd}-based electrochemical surface area (ECSA). Cyclic voltammetry (CV) was performed in the potential range of 0.05–0.925 V_{RHE} (50 cycles) with a sweep rate of 100 mV/s in N_2-saturated 0.1 M $HClO_4$ electrolyte to obtain a stable voltammogram. Then, three CV cycles were performed in the same potential range with a scan rate of 20 mV/s. The third cycle was used to determine the H_{upd}-based ECSA by integrating the hydrogen adsorption charge from 0.05–0.4 V_{RHE}. The internal resistance (IR) was determined by potential electrochemical impedance spectroscopy (PEIS) after applying a potential of 0.5 V_{RHE} for 5 min.

Oxygen reduction reaction (ORR) activities. Before the ORR measurements were performed in O_2 saturated 0.1 M $HClO_4$ solution, the background current was determined in N_2 saturated 0.1 M $HClO_4$ solution. The activity of the catalyst was extracted by linear sweep voltammetry (LSV) in the potential range of 0.05–1 V_{RHE} (anodic scan) with a rotational speed of 1600 rpm. The scan rate was 20 mV/s. The measurement was repeated 3 times.

ECSA based on CO-stripping. To obtain the ECSA based on CO-stripping, the working electrode was placed in the N_2-saturated electrolyte with a rotation speed of 400 rpm at 0.05 V_{RHE}. After CO gas was injected for 1 min, N_2 was injected into the solution for 10 min to remove the dissolved CO. Then, in steady state mode, CV was recorded between 0.05–1 V_{RHE} at 50 mV/s for 3 cycles. The ECSA was determined based on Q_{CO} obtained by integrating the area of the CO-stripping peak (approximately 0.4–1 V_{RHE}).

Accelerated stress tests (ASTs) were performed in 0.1M $HClO_4$ and N_2-saturated electrolyte. CV included 10,800 cycles in the potential range of 0.6–0.95 V_{RHE} with a scan rate of 500 mV/s. For PtNi(Mo)/C-17, 10,800, 15,800 and 22,800 cycles were performed, to study the long term stability of the catalysts. Correction of the data.

For LSV and CV measurements, the potential was corrected to the value on the RHE scale.

$$E_{RHE} = E_{measured} + E_{calibration} \tag{1.1}$$

Then, the potential (E) was IR corrected with the resistance obtained from PEIS.

$$E = E_{RHE} - IR \tag{1.2}$$

The background corrected current I_{ORR} was obtained by subtracting the current of the nitrogen saturated LSV I_{N2}.

$$I_{ORR} = I_{O_2} - I_{N_2} \tag{1.3}$$

Results and discussion

Syntheses of Oh-PtNi(Mo) NPs

Oh-PtNi(Mo) NPs with a mean edge length distribution of 5.5, 13.1, and 17.1 nm were prepared and subsequently supported on high surface area carbon, based on a synthesis recently reported.[38,39] Hereafter, the samples will be referred to as oh-PtNi(Mo)-L, where L is the mean edge length of the particles in nm. For the preparation of oh-PtNi(Mo)-13, we used a pressure-tight glass vessel for 12 h at 150 ℃ with BA, Pt and Ni acetylacetonate precursors and $Mo(CO)_6$ precursor. Following the first cleaning cycle, the supernatant showed a yellowish clear color corresponding to Pt precursors. After analyzing the supernatant for Pt and Ni contents, we found that the yield of the synthesis was around 50%. The size manipulation was achieved by interfering with the instantaneous nucleation or growth stages by releasing the products that build up the pressure and further shifting the reaction equilibrium to the product side. To increase the size of the active facets, we affected the growth stage by releasing the pressure that builds up as the precursors are reduced (P= 0.6 bar at 4 h). In this way, we produced octahedra with 17.1 nm edge length by shifting the equilibrium further to the side during the growth regime. We found that the timing of depressurization is of great importance. When the pressure was released at 2 h (P= 0.5 bar), the resulting particle size was smaller (5.5 ± 0.6 nm) compared to the synthesis without pressure release. This could indicate that nucleation still occurs after 2 h and the addition of new atoms increases the supersaturation concentration and resulted in a smaller particle size.[40] The schematic representation of the LaMer model and the adjustments described in this work are shown in Figure 1. We also performed the synthesis without $Mo(CO)_6$ precursor and depressurized the gas phase during the growth stage to prepare a relatively large Ni-rich oh-PtNi catalyst with an average edge length of 13 nm. The difference between 17 and 13 nm could be due to CO ligands saturating the gas phase at the beginning of the reaction and leading to a larger particle size (Figure S2).

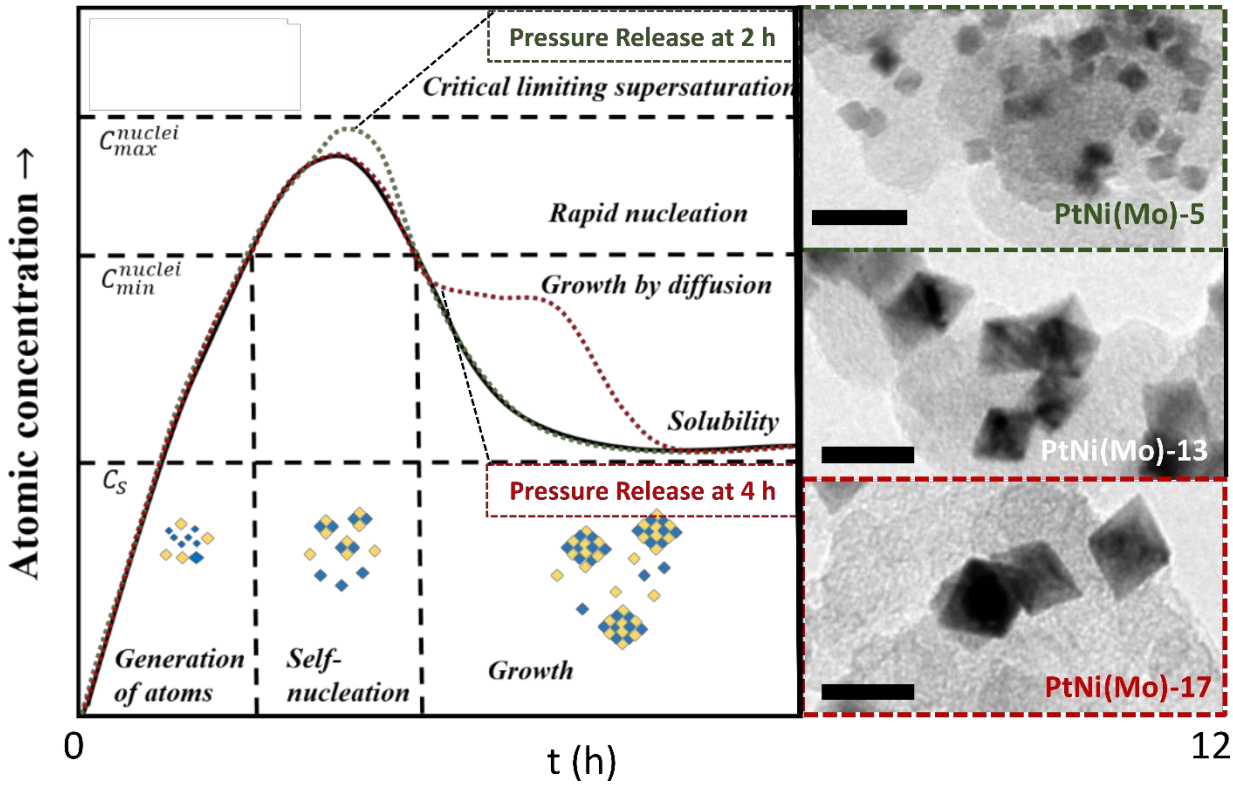

Figure 1. Classic schematic representation of the LaMer model/hypothesis for the formation of colloidal particles, adopted partially from the original 1950 paper.[31] Copyright 1950 American Chemical Society. The hypothetical curves display qualitatively the change in concentration of the soluble monomers as a function of time throughout the formation process. Black line corresponds to the synthesis without depressurizing. Green and red dashed lines represent the adjustments done in this work, green for depressurizing in the nucleation stage (2 h) and red for depressurizing in the growth stage (4 h). In the insets, TEM images of the resulting NPs. C_s is the saturation concentration. C_{min} is the critical supersaturation concentration required for nucleation; C_{max} is the limiting supersaturation. Postulated stage I: formation of the soluble monomer in solution. Postulated stage II: nucleation from solution when the monomer concentration is higher than C_{min}. At the postulated stage III, the monomer concentration falls below the level required for nucleation and particle growth continues by deposition of the monomer to particles surface. The scale bars correspond to 20 nm.

Structural and morphological characterization of the as-prepared catalysts

Transmission electron micrographs in Figure S3 show the as-prepared oh-NPs, which have a well-defined octahedral shape and a narrow size distribution of edge lengths. It should be pointed out that oh-PtNi(Mo)-5 NPs are Pt-rich and oh-PtNi(Mo)-13 and -17 NPs are Ni-rich. This is due to the reduction of more Pt precursors in the nucleation stage, which saturate the pressure phase and suppresses the equilibrium shift to the product side. The averaged PSD values, atomic composition and Ptw% are shown in Table S1.

X-ray diffraction (XRD) was used to investigate the crystal phase of the as-prepared NPs (Figure S4a). The XRD patterns show an increasing crystal structure complexity (peak multiplicity) with increasing nanoparticles size. Rietveld refinement analysis showed that oh-PtNi(Mo)-5 is composed of a single face-

centered cubic (FCC) phase with at % $Pt_{79}Ni_{21}$ according to its lattice constant and Vegard's law. oh-PtNi(Mo)-13 consisted of two FCC phases containing $Pt_{83}Ni_{17}$ and $Pt_{62}Ni_{38}$, respectively, with the latter phase accounting for about 68.1 wt% of the crystalline material. Oh-PtNi(Mo)-17 was best described by three phases of $Pt_{82}Ni_{18}$, $Pt_{58}Ni_{42}$ and $Pt_{21}Ni_{79}$, accounting for 29.4, 58.2 and 12.4 wt% of the crystalline material, respectively (Figure S4b–d). The Rietveld refinement results for the different as-prepared PtNi(Mo) NPs are listed in Table S1. Previous studies have reported an element-specific anisotropic growth mechanism of oh-PtNi NPs, in which rapid growth of Pt-rich hexapods/concave octahedra along the <100> directions is preceded by delayed deposition of the Ni-rich phase at the concave (111) sites, as in conventional one-pot syntheses.[10,41] oh-PtNi(Mo)-5 and -13 XRD deconvoluted phases correspond to the previously reported elemental segregation on Pt-rich and Ni-rich octahedra.[39]

To elucidate the morphology and compositional profile at atomic resolution for the exceptional large octahedra, we studied the as-prepared oh-PtNi(Mo)-17 NPs using a FEI Titan-80-200 scanning transmission electron microscope. Non-negative matrix factorization (NMF) was performed and the data was decomposed into principal components. Recombination of these components produced a 'de-noised' dataset from which the elemental maps were extracted. The Pt and Ni maps were then quantified (Mo content was too low for accurate quantification) using the EDS partial cross section approach and calibrated standards.[42,43] All of this analysis was performed using the open source Python-based software Hyperspy.[44] Figure 2a shows ADF-STEM images and corresponding EDS elemental maps of the as-prepared oh-PtNi(Mo)-17 NPs, whilst Figure 2b shows the output components from the NMF analysis. The EDS analysis of oh-PtNi(Mo)-17 shows an elemental distribution consisting of three distinct, separated regions of a Pt-rich phase in the form of a concave octahedron core surrounded by apexes of lower Pt content and Ni-rich facets and edges. The three different regions correspond well to the XRD phase analysis. However, the extracted sizes of the XRD phases show a corresponding trend, but smaller sizes. This could be due to the isotropic (spherical) NPs model rather than the octahedral NPs model used for the XRD peaks deconvolution. The deposition of the Ni-rich edges and facets is unique and likely due to the release of pressure that led to further reduction of precursors, mainly Ni, at this stage of growth (Figure S5).

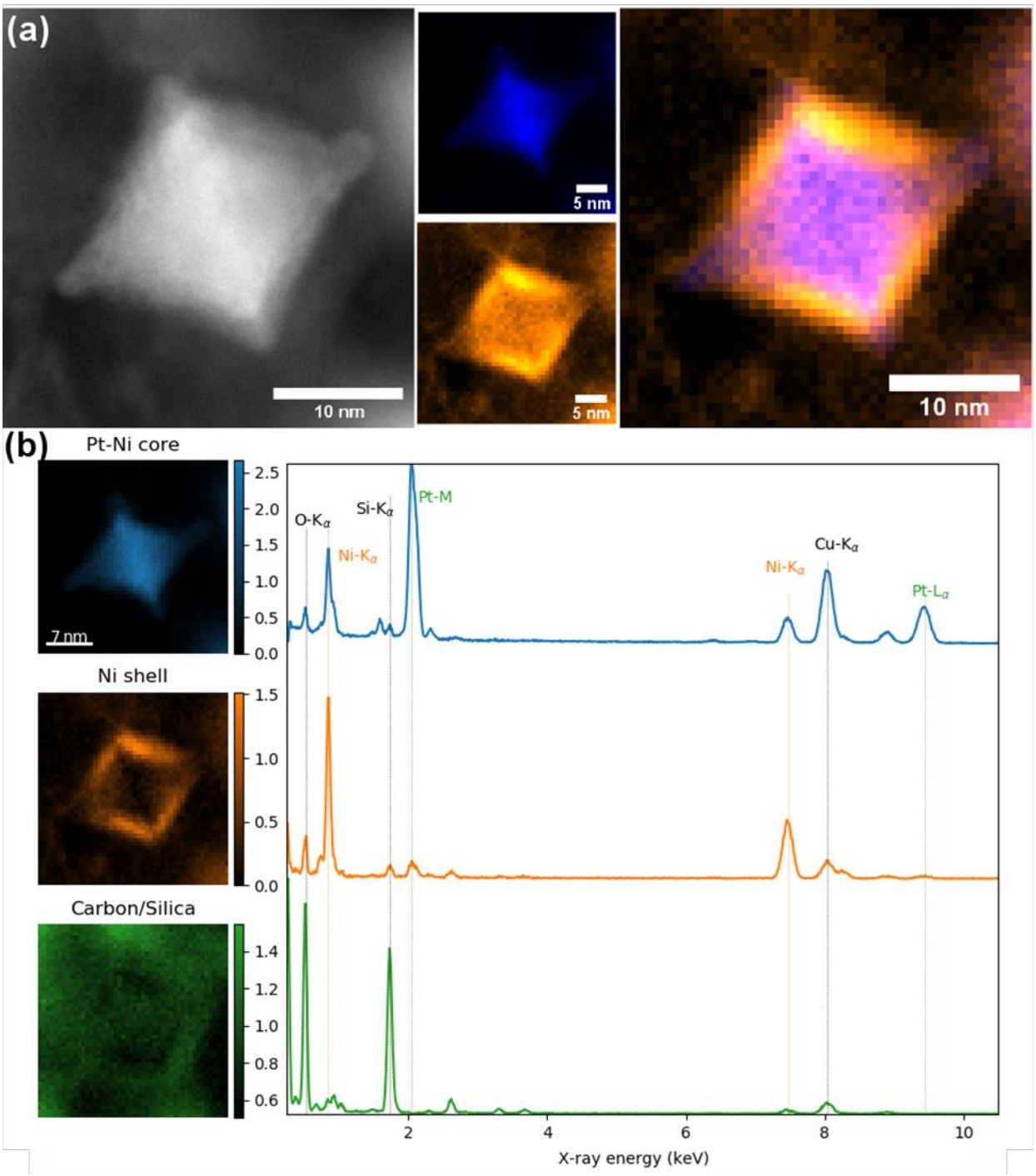

Figure 2. As-prepared oh-PtNi(Mo)-17: (a) ADF-STEM micrograph, STEM-EDS elemental mapping for Pt (blue) and Ni (yellow), and their overlay imaged along a <110> direction (see supplementary Figure S6 for <100> direction). (b) The STEM-EDS results are analyzed in more detail using non-negative matrix factorization (NMF) showing the output components. The three EDS component maps and corresponding spectra show the distribution of a Pt-rich core (blue), a Ni- and O-rich shell (orange), as well as C, O, and Si (green).

Structural and morphological transformations during thermal annealing

Following the synthesis, we thermally annealed the oh-PtNi(Mo)-17 catalyst using in situ high-temperature XRD at 350 ℃ under reducing or oxidizing atmospheres (H_2:Ar, 4:96% or air, respectively, for 30 min hold and 56 min more for the scan, Figure S1) to investigate the influence of different adsorbates on element segregation and tailor the catalyst surface by inducing small variations in the surface−reactant binding energies, which could considerably enhance the catalytic ORR activity and stabillity.[33,35] For the H_2-annealed oh-PtNi(Mo)-17 (hereafter PtNi(Mo)-17H) sample, a shift of the (111) peak to lower 2θ values was observed only in the scan at 350 ℃, which is expected due to the increase of the lattice parameter (Figure 3).[35] The XRD patterns at 350 ℃ and room temperature after annealing show a transformation of the shoulder in the (111) peak to a distinct peak at higher 2θ values. This behavior of the (111) peak strongly suggests the formation of a Ni-rich phase on the surface of the as-prepared oh-PtMi(Mo)-17. In the air-annealed oh-PtNi(Mo)-17 sample (hereafter PtNi(Mo)-17A), the (111) peak shifted to lower 2θ values in the 350 ℃ pattern and after annealing, accompanied by the formation of a more symmetrical peak due to the loss of the shoulder at higher 2θ values. This shift to lower 2θ values indicated the formation of a Pt-Ni phase that is enriched with Pt.

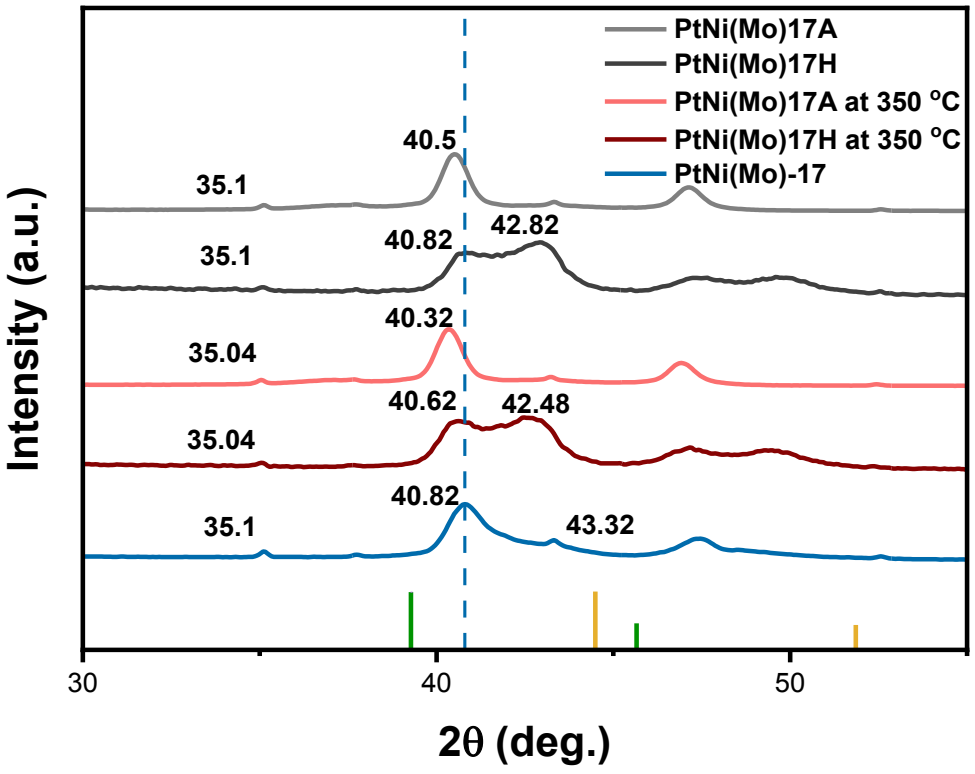

Figure 3. In situ heating XRD experiment, showing the evolution of the (111) and (200) reflections for the oh-PtNi(Mo)-17 sample upon exposure to either reductive (H_2:Ar, 4:96%) or oxidizing (air) atmosphere at 350 °C. The green lines correspond to the pure Pt (PDF No. 00-004-0802) and the orange lines to the pure Ni patterns (PDF No. 00-004-0850). The peaks around 35.1 and 43.3 2θ values correspond to the Al_2O_3 peaks of the high-temperature holder.

The TEM image of the air-annealed sample shows an octahedral core@shell structure with a darker core and a brighter shell (Figure S7a). On the other hand, the air-annealed TEM image of the H_2-annealed sample shows the transformation to a distorted octahedron accompanied with the facet-to-facet coalescence of neighboring octahedral particles and the formation of agglomerates of several octahedra as well (Figure S7b).[45] Development of an external oxide shell in the air-annealed samples protects the particles from coalescing.

The air-annealed particles were also investigated using high-resolution STEM, corresponding ADF images and EDS elemental maps are shown in Figures 4a and S8. Figures 4b and S9 show the output components from the NMF EDS analysis and the elemental maps, respectively. The ADF images show the core@shell structure in high resolution. The high resolution STEM-EDS elemental analysis of PtNi(Mo)-17A demonstrates the formation of a thick Nickel-oxide-rich shell with no Pt detected in this region. This is consistent with the absence of an amorphous Nickel oxide phase in the XRD patterns produced using the laboratory HT-XRD system. These results are consistent with previous studies showing the progressive segregation of Ni on the surface of Pt-Ni NPs and the associated formation of Nickel oxide species when annealed in an oxygen environment.[46–48] After thermal annealing in air, PtNi(Mo)-17A is electrochemically inactive for ORR, as expected from Nickel oxide surfaces.

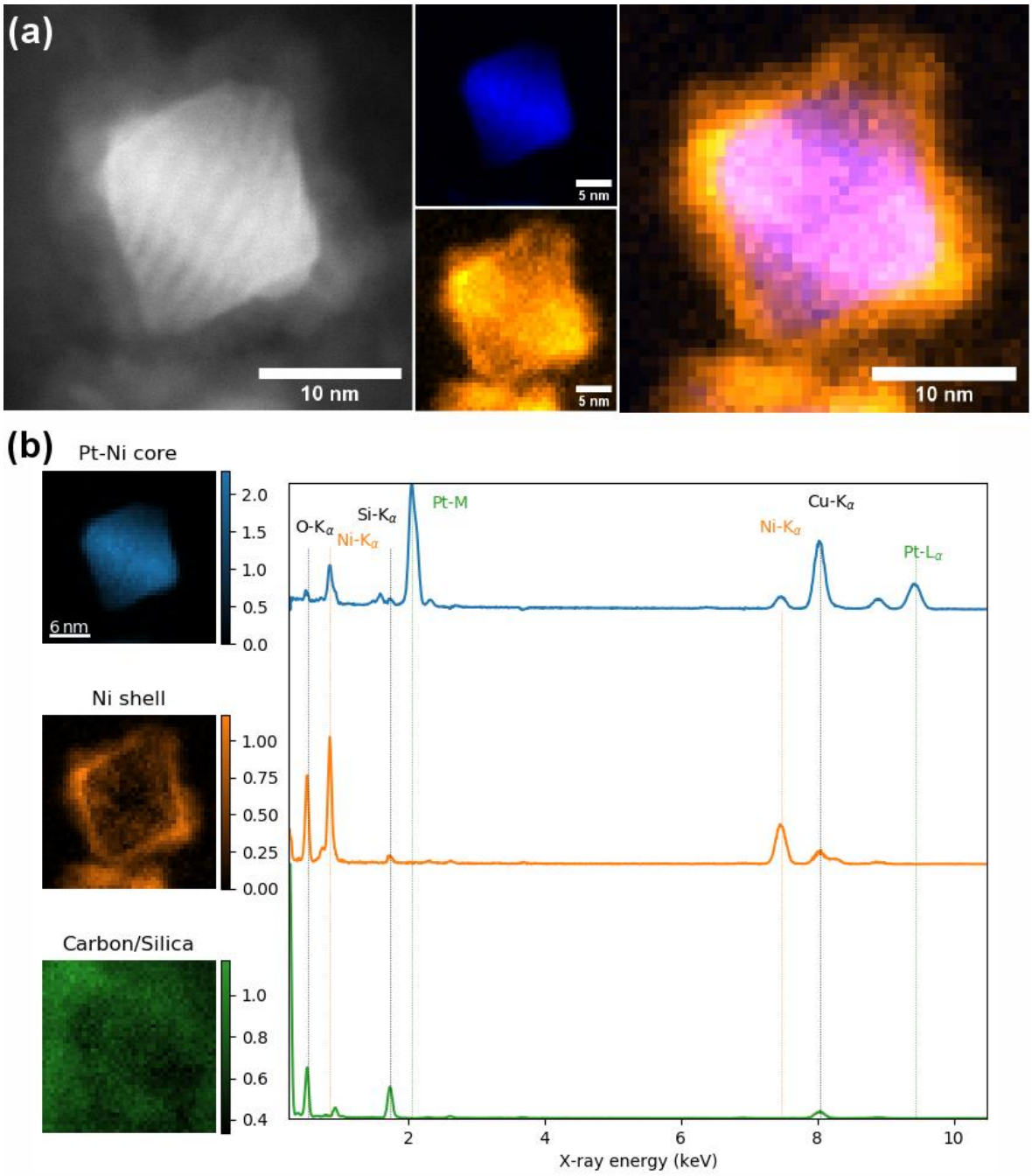

Figure 4. Air-annealed PtNi(Mo)-17A: (a) ADF-STEM micrograph, STEM-EDS elemental mapping for Pt (blue) and Ni (yellow), and their overlay, imaged along a <110> direction (see supplementary Figure S8 for <100> direction). (b) EDS NMF component maps and corresponding spectra show the distribution of a Pt-rich core (blue), a Ni- and O-rich shell (orange), as well as C, O, and Si (green).

For the H_2-annealed sample, Figure 5a shows ADF-STEM images and corresponding EDS elemental maps of PtNi(Mo)-17H NPs, while Figure 5b shows the 4 output components of the NMF analysis. PtNi(Mo)-17H shows a rounded octahedron with a Pt-rich core and a Ni-rich shell. Compared to Pt, Ni has a higher affinity for oxygen, NiO_x formation energy of -2.54 eV per O compared to PtO, PtO_2 formation energies of -0.41 and -0.63 eV per O.[49] This could be the reason why the as-prepared NPs exhibit oxygen enrichment at the surface and subsurface of the particles. Previous studies have shown that annealing under reducing atmospheres leads to segregation of the nickel surface until significant oxide decomposition is reached, which occurs above 200 °C in H_2. This segregation is restricted to a few atomic layers near the surface and generally leads to the formation of a sandwich or Pt-skin structure in which the outermost atomic layer is Pt-rich and the second layer is Ni-rich. A short-range atomic exchange near the surface, where Pt atoms in the second layer exchange places with Ni atoms on the surface, could explain how such a structure can be achieved.[47]

Figure S10 shows elemental maps of the as-prepared, H_2- and air-annealed PtNi(Mo)-17, after NMF analysis, for O, Ni and Pt plotted on the same intensity scale viewed along the <100> direction. It can be seen that the O intensities are highest for the as-prepared and the air-annealed NPs and barely noticeable for the H_2-annealed NP, confirming the presence of a Nickel oxide shell in the as-prepared sample. The reduction of the Nickel oxide shell and the formation of a Ni-rich shell is consistent with the observation of an additional (111) peak in the XRD experiments during and after H_2-annealing.

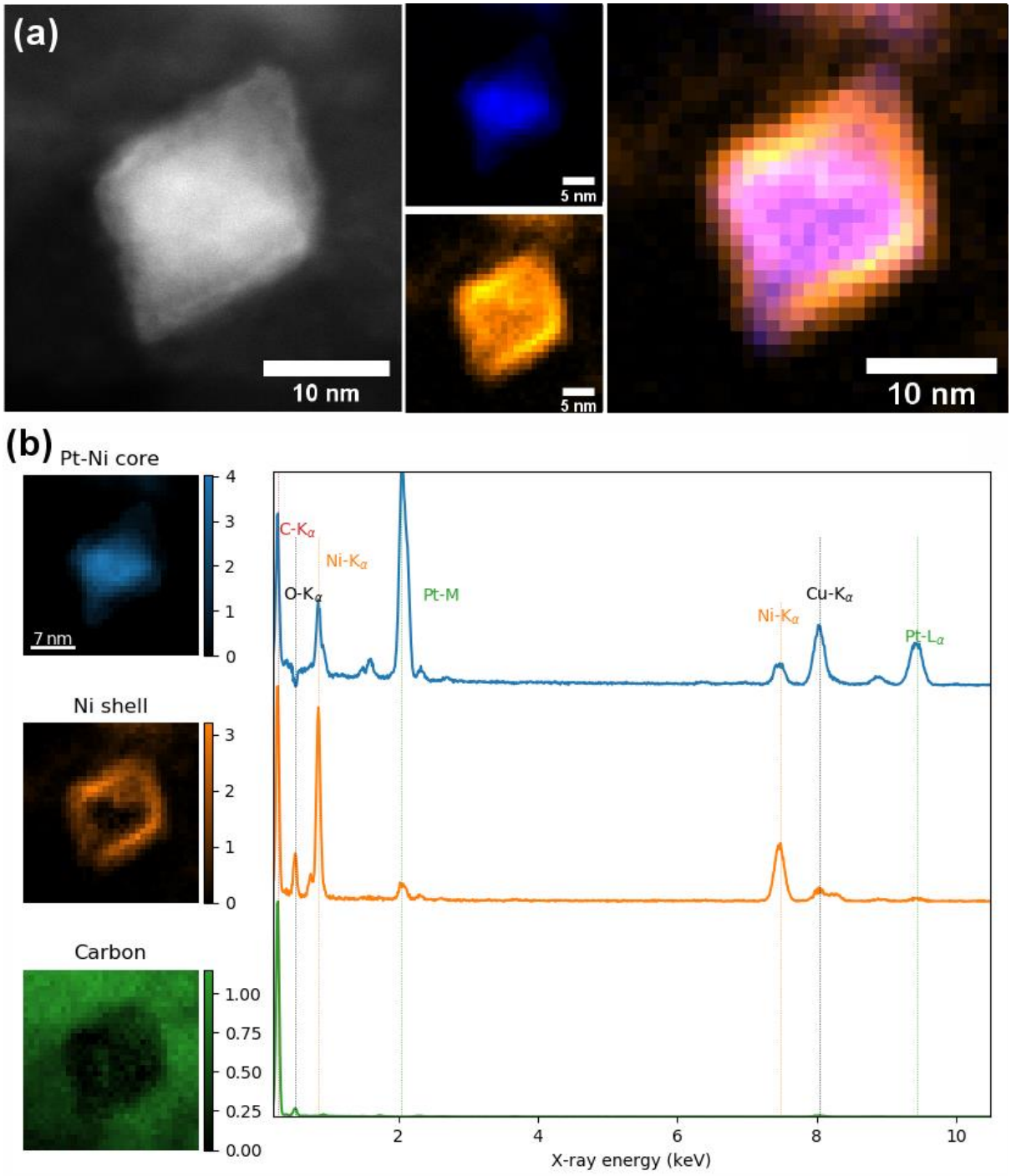

Figure 5. H_2-annealed PtNi(Mo)-17H: (a) ADF-STEM micrograph, STEM-EDS elemental mapping for Pt (blue) and Ni (yellow), and their overlay, imaged along a <110> direction (see supplementary Figure S11 for <100> direction). (b) EDS NMF component maps and corresponding spectra show the distribution of a Pt-rich core (blue), a Ni- and O-rich shell (orange), as well as C (green).

Electrocatalytic ORR activities and CO oxidation reaction

To illustrate the compositional evolution of octahedral surface and subsurface layers, we deconvolved the CO-stripping curves of the different catalysts before and after ASTs into different regions. Based on previous CO-stripping studies, it has been shown that the oxidation properties of CO, adsorbed on the surface of Pt-based NPs, are structure sensitive and lead to peak multiplication.[50] In Figure 6c and 6d, we assign the pre-peak at 0.35−0.6 V_{RHE} to the (111) and the (100) facets, peak 1a exclusively to the (111) facet (0.68−0.7 V_{RHE}), and peak 1b to the low coordination sites (0.7−0.72 V_{RHE}). Peak 1a emerges in oh-PtNi(Mo)-17 and is more evident in the PtNi(Mo)-17H pattern, but is absent in the oh-PtNi(Mo)-5 and oh-PtNi(Mo)-13 patterns, due to a bigger portion of under coordinated sites in edges and vertexes. The pre-peak and peak 1a, have also been seen in the adsorption properties of annealed PtNi core@shell NPs with a Pt-skin-type surface and well-defined skin-type extended surfaces of $Pt_3Ni(111)$.[51] Moreover, peak 1a is absent in the deconvolution products of all patterns after ASTs. TEM images of oh-PtNi(Mo)-13, oh-PtNi(Mo)-17 and PtNi-17H after ASTs show the presence of concave octahedra (Figure 6). The electrochemical surface areas (ECSAs) of the PtNi(Mo) series were measured by hydrogen underpotential deposition (H_{UPD}) and the CO-stripping method (Figures 6 and S12). The oh-PtNi(Mo)-5 catalyst exhibits the highest CO-based ECSA and the value decreases with increasing particle size, an expected trend (Figure 7a). Vliet et al.[51] reported that the charge ratio of CO to H_{upd} ($Q_{CO}/2Q_H$), may have some qualitative predictive power regarding the Pt-to-Ni composition at the surface/subsurface layers. $Q_{CO}/2Q_H$ values close to unity indicate a thick Pt shell or Pt-rich surface, a pure Pt, or a uniform distribution of Pt and Ni, while values closer to 1.5 indicate a Pt-skin-type surface. For all catalysts in the initial state, we calculated a $Q_{CO}/2Q_H$ ratio between 1−1.3 (Figure 7b).

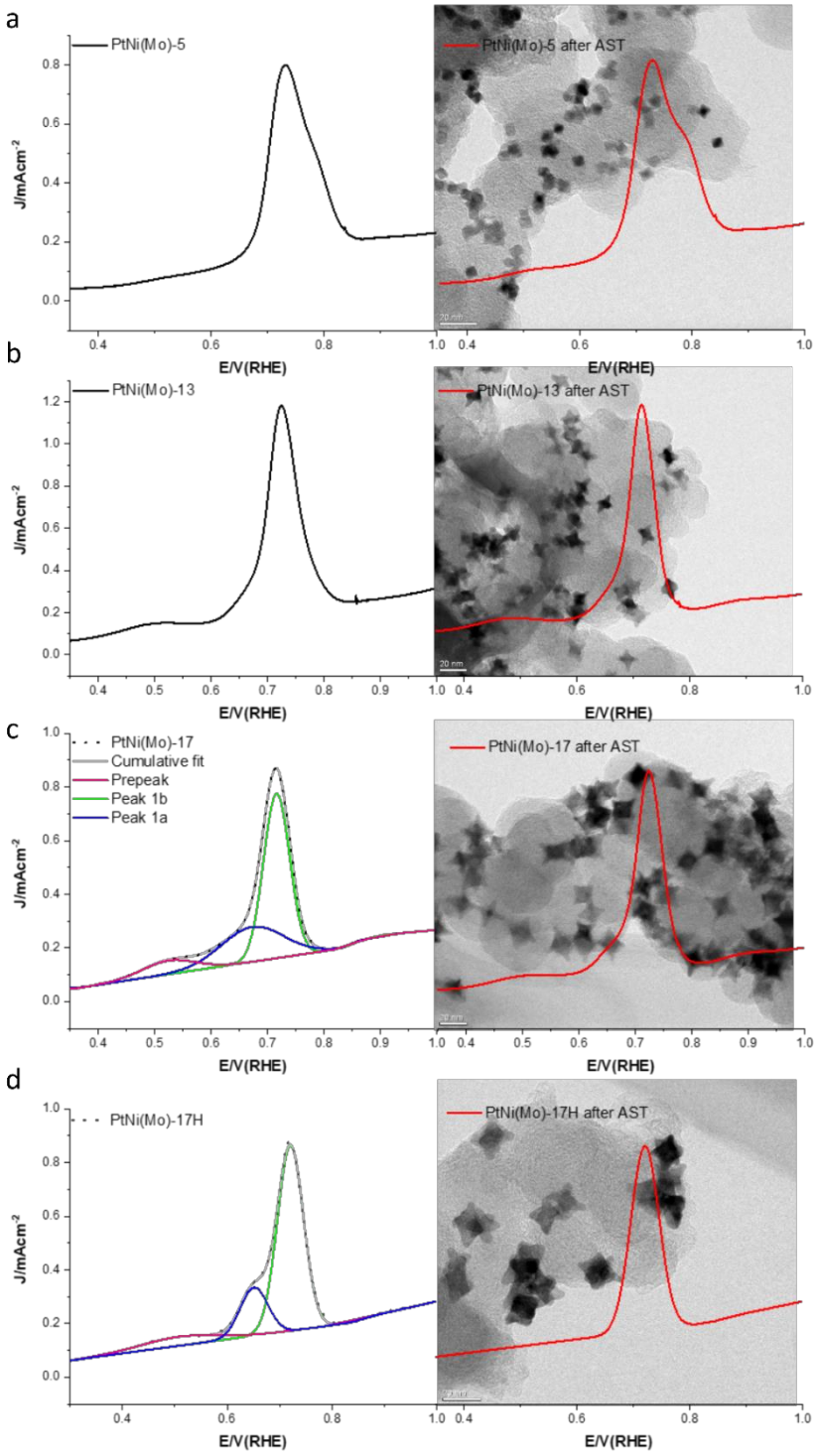

Figure 6. CO-stripping analysis of the surface structures and adsorption properties. (left) Initial CO-stripping curve, (right) TEM images after 10.8k cycles of AST and the corresponding CO-stripping curve and deconvolution products of the curve for (a) oh-PtNi(Mo)-5, (b) oh-PtNi(Mo)-13, (c) oh-PtNi(Mo)-17 and (d) PtNi(Mo)-17H catalysts.

For the PtNi(Mo)-17H catalyst before AST, a calculated $Q_{CO}/2Q_H$ ratio of about 1.35 was measured, indicating the development of the so-called Pt-skin-type surface.[51] We recorded cyclic voltammetry (CV) curves for the catalysts in N_2-purged 0.1 M $HClO_4$ electrolyte for activation, to remove trace amounts of PVP from the surface,[52] and to measure $ECSAs_{Hupd}$. This was followed by linear sweep voltammetry (LSV) measurements in O_2-saturated electrolyte (Figures S12 and S13). The SAs (CO-based) and MAs before ASTs are relatively high, and show no correlation with particle size. The total difference in $ECSA_{CO}$ for all catalysts is about 10 $m^2\ g_{Pt}^{-1}$, which is smaller than expected for this size range. In a spherical pure Pt catalyst or bimetallic M@Pt with a Pt shell, the sizes should correlate with the ECSAs. However, in an oh-PtNi catalyst, the situation is more complex due to the specific elemental segregation of Pt-rich hexapod and Ni-rich facets and shell. Moreover, Pt and Ni segregation also correlates with the size of the particles and composition, further complicating the situation.[39,53] PtNi(Mo)-5 and PtNi(Mo)17H show increased $ECSA_{Hupd}$ after ASTs, which could be due to atomic rearrangement at the surface during ASTs. Nevertheless, PtNi(Mo)-5 and PtNi(Mo)17H show decreased SAs after ASTs. In contrast, PtNi(Mo)-5 and PtNi(Mo)17H show almost the same $ECSA_{CO}$ value before and after ASTs. This could be due to the finding that the $ECSAs_{Hupd}$ are typically smaller than the $ECSAs_{CO}$ and their use could overestimate the actual specific ORR activity.[37] The stability of oh-PtNi(Mo)-5, the smallest catalyst, is good as it retains almost all of its MA. Oh-PtNi(Mo)-13 shows an improved SA after AST, but with a slight decrease in MA.

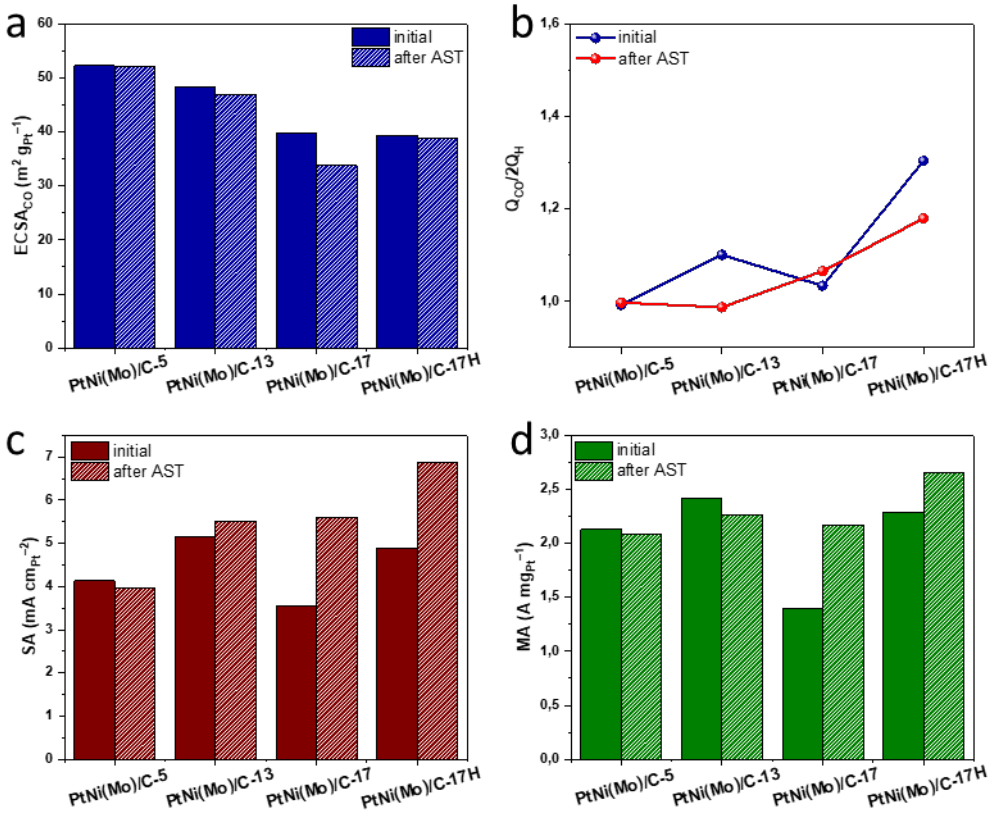

Figure 7. Electrochemical performance and stability of the as-prepared PtNi(Mo) series (a) CO-based ECSA before and after 10.8k AST cycles, (b) $Q_{CO}/2Q_H$, (c) SAs before and after 10.8k AST cycles and (d) MAs before and after 10.8 AST.

After 10.8k AST cycles, oh-PtNi(Mo)-17 showed significantly improved mass and specific activities accompanied by 84.7% ECSA retention. Additional testing was carried out on the oh-PtNi(Mo)-17 catalyst at 15.8k and 22.8k cycles to evaluate its long-term stability. Figure S14a presents the ORR polarization curves after selected cycles, the inset shows a magnification of the potentials at which the activities were sampled (0.9 and 0.95 V_{RHE}). After 10.8k, 15.8k and 22.8k AST cycles, oh-PtNi(Mo)-17 MA increased by 131, 132 and 117%, respectively, from its initial MA (1.35 A mg_{Pt}^{-1}, Figure S14b). In Figure 7c, the SAs after ASTs show an increasing trend that correlates with the octahedral size, with the H_2-annealed catalysts PtNi(Mo)-17H showing the highest specific and mass activities after AST in this work, reaching SA and MA of 6.87 mA cm_{Pt}^{-2} and MA of 2.65 A mg_{Pt}^{-1} (about 15 and 8.5 times higher than Pt/C, respectively).

We also tested oh-PtNi-13, PtNi(Mo)-5H, and PtNi(Mo)-13H for their electrochemical performance and stability. For oh-PtNi-13 catalysts, the MAs before and after the AST are about 60% of the MAs of PtNi(Mo)-17H. For PtNi(Mo)-5H, the activity was very low, possibly due to the complete loss of shape and significant coalescence of many particles after the H_2-annealing (Figure S15). It should be noted that the optimum temperature for 8 nm oh-$PtNi_{1.5}$, which shows the best performance, is 300 °C.[36] For PtNi(Mo)-13H, the activities were relatively the same. However, the highest activity for PtNi(Mo)-13H was actually obtained at 300 °C.

Conclusions

Size-selected oh-PtNi(Mo)-L octahedral catalysts were synthesized in a sealed pressure flask. Depressurization in the nucleation stage resulted in a large spontaneous nucleation burst leading to small Pt-rich octahedra, while depressurization in the growth stage resulted in large octahedra that exhibited a Pt-rich core surrounded by Ni-rich facets and edges, and a moderate Pt:Ni levels in vertices. We investigated the atomic segregation phenomena of Ni-rich large Mo-doped oh-PtNi catalysts before and after annealing in reducing or oxidizing gas environments. The as-prepared catalysts and those annealed in air exhibited a relatively thick Nickel oxide shell, while the catalysts annealed in H_2 showed a reduction of the Nickel oxide phase and the development of a so-called Pt skin-type surface. These structural changes and the formation of a Pt-skin was accompanied by high performance and an increased activity after the stability test. Our results show that manipulating the reaction equilibrium at different stages of nucleation and growth in reactions involving gas products carried out in a sealed pressure flask, serves as a method to broaden the size window and also to control the atomic structure of the catalyst surface. These results could facilitate the use of a new class of relatively large and stable Mo-doped oh-PtNi catalysts for use in PEMFCs the cathodes.

ASSOCIATED CONTENT

AUTHOR INFORMATION

Corresponding Authors

pstrasser@tu-berlin.de
m.heggen@fz-juelich.de
polani@tu-berlin.de

Author Contributions

The manuscript was written through contributions of all authors. All authors have given approval to the final version of the manuscript.

Funding Sources

The authors are grateful for the financial support by the Deutsche Forschungsgemeinschaft (DFG) under the grant numbers HE 7192/1-2, STR 596/5-2 and STR 596/18-1. R.C. received financial support from the European Union's Horizon 2020 research and innovation programme, Fuel Cells and Hydrogen 2 Joint Undertaking under the GAIA project, Grant Agreement No. 826097.

Supporting Information. TEM images, STEM-EDS, XRD and deconvolution data, CV curves, ORR polarization curves are provided. This material is available free of charge via the Internet at http://pubs.acs.org.

ACKNOWLEDGMENT

References

(1) Sun, Y.; Polani, S.; Luo, F.; Ott, S.; Strasser, P.; Dionigi, F. Advancements in Cathode Catalyst and Cathode Layer Design for Proton Exchange Membrane Fuel Cells. *Nature Communications*. Springer US 2021, pp 1–14. https://doi.org/10.1038/s41467-021-25911-x.

(2) Cullen, D. A.; Neyerlin, K. C.; Ahluwalia, R. K.; Mukundan, R.; More, K. L.; Borup, R. L.; Weber, A. Z.; Myers, D. J.; Kusoglu, A. New Roads and Challenges for Fuel Cells in Heavy-Duty Transportation. *Nat. Energy* **2021**, *6* (5), 462–474. https://doi.org/10.1038/s41560-021-00775-z.

(3) Marković, N. M.; Adžić, R. R.; Cahan, B. D.; Yeager, E. B. Structural Effects in Electrocatalysis: Oxygen Reduction on Platinum Low Index Single-Crystal Surfaces in Perchloric Acid Solutions. *J. Electroanal. Chem.* **1994**, *377* (1–2), 249–259. https://doi.org/10.1016/0022-0728(94)03467-2.

(4) Stamenkovic, V. R.; Mun, B. S.; Arenz, M.; Mayrhofer, K. J. J.; Lucas, C. A.; Wang, G.; Ross, P. N.; Markovic, N. M. Trends in Electrocatalysis on Extended and Nanoscale Pt-Bimetallic Alloy Surfaces. *Nat. Mater.* **2007**, *6* (3), 241–247. https://doi.org/10.1038/nmat1840.

(5) Stamenkovic, V.; Mun, B. S.; Mayrhofer, K. J. J.; Ross, P. N.; Markovic, N. M.; Rossmeisl, J.; Greeley, J.; Nørskov, J. K. Changing the Activity of Electrocatalysts for Oxygen Reduction by Tuning the Surface Electronic Structure. *Angew. Chemie Int. Ed.* **2006**, *45* (18), 2897–2901. https://doi.org/10.1002/anie.200504386.

(6) Escudero-Escribano, M.; Malacrida, P.; Hansen, H. M.; Vej-Hansen, U.; Velazquez-Palenzuela, A.; Tripkovic, V.; Schiøtz, J.; Rossmeisl, J.; Stephens, I. E. L.; Chorkendorff, I. Tuning the Activity of Pt Alloy Electrocatalysts by Means of the Lanthanide Contraction María. *Science (80-.).* **2016**, *352* (6281), 73–76.

(7) Polani, S.; Shviro, M.; Shokhen, V.; Zysler, M.; Glüsen, A.; Dunin-Borkowski, R.; Carmo, M.; Zitoun, D. Size Dependent Oxygen Reduction and Methanol Oxidation Reactions: Catalytic Activities of PtCu Octahedral Nanocrystals. *Catal. Sci. Technol.* **2020**, *10* (16), 5501–5512.

https://doi.org/10.1039/d0cy00772b.

(8) Stamenkovic, V. R.; Strmcnik, D.; Lopes, P. P.; Markovic, N. M. Energy and Fuels from Electrochemical Interfaces. *Nature Materials*. 2016, pp 57–69. https://doi.org/10.1038/nmat4738.

(9) Strasser, P. Catalysts by Platonic Design. *Science (80-.).* **2015**, *349* (6246), 379–380. https://doi.org/10.1126/science.aac7861.

(10) Cui, C.; Gan, L.; Heggen, M.; Rudi, S.; Strasser, P. Compositional Segregation in Shaped Pt Alloy Nanoparticles and Their Structural Behaviour during Electrocatalysis. *Nat. Mater.* **2013**, *12* (June), 1–7. https://doi.org/10.1038/NMAT3668.

(11) Huang, X.; Zhao, Z.; Chen, Y.; Zhu, E.; Li, M.; Duan, X.; Huang, Y. A Rational Design of Carbon-Supported Dispersive Pt-Based Octahedra as Efficient Oxygen Reduction Reaction Catalysts. *Energy Environ. Sci.* **2014**, *7* (9), 2957–2962. https://doi.org/10.1039/c4ee01082e.

(12) Zhu, E.; Li, Y.; Chiu, C. Y.; Huang, X.; Li, M.; Zhao, Z.; Liu, Y.; Duan, X.; Huang, Y. In Situ Development of Highly Concave and Composition-Confined PtNi Octahedra with High Oxygen Reduction Reaction Activity and Durability. *Nano Res.* **2016**, *9* (1), 149–157. https://doi.org/10.1007/s12274-015-0927-3.

(13) Wang, J.; Li, B.; Gao, X.; Yang, D.; Lv, H.; Xiao, Q.; Kær, S. K.; Zhang, C. From Rotating Disk Electrode to Single Cell: Exploration of PtNi/C Octahedral Nanocrystal as Practical Proton Exchange Membrane Fuel Cell Cathode Catalyst. *J. Power Sources* **2018**, *406* (October), 118–127. https://doi.org/10.1016/j.jpowsour.2018.10.010.

(14) Zhang, J.; Yang, H.; Fang, J.; Zou, S. Synthesis and Oxygen Reduction Activity of Shape-Controlled Pt 3Ni Nanopolyhedra. *Nano Lett.* **2010**, *10* (2), 638–644. https://doi.org/10.1021/nl903717z.

(15) Wu, J.; Gross, A.; Yang, H. Shape and Composition-Controlled Platinum Alloy Nanocrystals Using Carbon Monoxide as Reducing Agent. *Nano Lett.* **2011**, *11* (2), 798–802. https://doi.org/10.1021/nl104094p.

(16) Choi, S. Il; Xie, S.; Shao, M.; Odell, J. H.; Lu, N.; Peng, H. C.; Protsailo, L.; Guerrero, S.; Park, J.; Xia, X.; Wang, J.; Kim, M. J.; Xia, Y. Synthesis and Characterization of 9 Nm Pt-Ni Octahedra with a Record High Activity of 3.3 A/MgPt for the Oxygen Reduction Reaction. *Nano Lett.* **2013**, *13* (7), 3420–3425. https://doi.org/10.1021/nl401881z.

(17) Shao, M.; Odell, J. H.; Choi, S. Il; Xia, Y. Electrochemical Surface Area Measurements of Platinum- and Palladium-Based Nanoparticles. *Electrochem. commun.* **2013**, *31*, 46–48. https://doi.org/10.1016/j.elecom.2013.03.011.

(18) Chou, S. W.; Lai, Y. R.; Yang, Y. Y.; Tang, C. Y.; Hayashi, M.; Chen, H. C.; Chen, H. L.; Chou, P. T. Uniform Size and Composition Tuning of PtNi Octahedra for Systematic Studies of Oxygen Reduction Reactions. *J. Catal.* **2014**, *309*, 343–350. https://doi.org/10.1016/j.jcat.2013.09.008.

(19) Wu, Y.; Cai, S.; Wang, D.; He, W.; Li, Y. Syntheses of Water-Soluble Octahedral, Truncated Octahedral, and Cubic Pt-Ni Nanocrystals and Their Structure-Activity Study in Model Hydrogenation Reactions. *J. Am. Chem. Soc.* **2012**, *134* (21), 8975–8981. https://doi.org/10.1021/ja302606d.

(20) Jia, Q.; Zhao, Z.; Cao, L.; Li, J.; Ghoshal, S.; Davies, V.; Stavitski, E.; Attenkofer, K.; Liu, Z.; Li, M.;

Duan, X.; Mukerjee, S.; Mueller, T.; Huang, Y. Roles of Mo Surface Dopants in Enhancing the ORR Performance of Octahedral PtNi Nanoparticles. *Nano Lett.* **2018**, *18* (2), 798–804. https://doi.org/10.1021/acs.nanolett.7b04007.

(21) Cao, L.; Mueller, T. Theoretical Insights into the Effects of Oxidation and Mo-Doping on the Structure and Stability of Pt-Ni Nanoparticles. *Nano Lett.* **2016**, *16* (12), 7748–7754. https://doi.org/10.1021/acs.nanolett.6b03867.

(22) Huang, X.; Cao, L.; Chen, Y.; Zhu, E.; Lin, Z.; Li, M.; Yan, A.; Zettl, A.; Wang, Y. M.; Duan, X.; Mueller, T. High-Performance Transition Metal – Doped Pt 3 Ni Octahedra for Oxygen Reduction ReactionHuang, X., Cao, L., Chen, Y., Zhu, E., Lin, Z., Li, M., … Mueller, T. (2015). High-Performance Transition Metal – Doped Pt 3 Ni Octahedra for Oxygen Reduction Reactio. *Science (80-.).* **2015**, *348* (6240), 1230–1234.

(23) Beermann, V.; Gocyla, M.; Willinger, E.; Rudi, S.; Heggen, M.; Dunin-Borkowski, R. E.; Willinger, M. G.; Strasser, P. Rh-Doped Pt-Ni Octahedral Nanoparticles: Understanding the Correlation between Elemental Distribution, Oxygen Reduction Reaction, and Shape Stability. *Nano Lett.* **2016**, *16* (3), 1719–1725. https://doi.org/10.1021/acs.nanolett.5b04636.

(24) Lim, J.; Shin, H.; Kim, M.; Lee, H.; Lee, K. S.; Kwon, Y.; Song, D.; Oh, S.; Kim, H.; Cho, E. Ga-Doped Pt-Ni Octahedral Nanoparticles as a Highly Active and Durable Electrocatalyst for Oxygen Reduction Reaction. *Nano Lett.* **2018**, *18* (4), 2450–2458. https://doi.org/10.1021/acs.nanolett.8b00028.

(25) Stamenkovic, V. R.; Fowler, B.; Mun, B. S.; Wang, G.; Ross, P. N.; Lucas, C. A.; Markovic, N. M. Improved Oxygen Reduction Activity on Pt3Ni(111) via Increased Surface Site Availability. *Science (80-.).* **2007**, *315* (5811), 493–497. https://doi.org/10.1126/science.1135941.

(26) Debe, M. K. Electrocatalyst Approaches and Challenges for Automotive Fuel Cells. *Nature*. Nature Publishing Group June 2012, pp 43–51. https://doi.org/10.1038/nature11115.

(27) Hubert A. Gasteiger and Nenad M Markovic. Just a Dream—or Future Reality? *Science (80-.).* **2009**, *324* (April), 1029–1031.

(28) Debe, M. K.; Schmoeckel, A. K.; Vernstrom, G. D.; Atanasoski, R. High Voltage Stability of Nanostructured Thin Film Catalysts for PEM Fuel Cells. *J. Power Sources* **2006**, *161* (2), 1002–1011. https://doi.org/10.1016/j.jpowsour.2006.05.033.

(29) Shao-Horn, Y.; Sheng, W. C.; Chen, S.; Ferreira, P. J.; Holby, E. F.; Morgan, D. Instability of Supported Platinum Nanoparticles in Low-Temperature Fuel Cells. *Top. Catal.* **2007**, *46* (3–4), 285–305. https://doi.org/10.1007/s11244-007-9000-0.

(30) Han, B.; Carlton, C. E.; Kongkanand, A.; Kukreja, R. S.; Theobald, B. R.; Gan, L.; O'Malley, R.; Strasser, P.; Wagner, F. T.; Shao-Horn, Y. Record Activity and Stability of Dealloyed Bimetallic Catalysts for Proton Exchange Membrane Fuel Cells. *Energy Environ. Sci.* **2015**, *8* (1), 258–266. https://doi.org/10.1039/c4ee02144d.

(31) Lamer, V. K.; Dinegar, R. H. Theory, Production and Mechanism of Formation of Monodispersed Hydrosols. *J. Am. Chem. Soc.* **1950**, *72* (11), 4847–4854. https://doi.org/10.1021/ja01167a001.

(32) Whitehead, C. B.; Özkar, S.; Finke, R. G. LaMer's 1950 Model for Particle Formation of Instantaneous Nucleation and Diffusion-Controlled Growth: A Historical Look at the Model's Origins, Assumptions, Equations, and Underlying Sulfur Sol Formation Kinetics Data. *Chem.*

Mater. **2019**, *31* (18), 7116–7132. https://doi.org/10.1021/acs.chemmater.9b01273.

(33) Mayrhofer, K. J. J.; Juhart, V.; Hartl, K.; Hanzlik, M.; Arenz, M. Adsorbate-Induced Surface Segregation for Core-Shell Nanocatalysts. *Angew. Chem. Int. Ed. Engl.* **2009**, *48* (19), 3529–3531. https://doi.org/10.1002/anie.200806209.

(34) Zhao, Q.; Wang, C.; Wang, H.; Wang, J.; Tang, Y.; Mao, Z.; Sasaki, K. H2-Induced Thermal Treatment Significantly Influences the Development of a High Performance Low-Platinum Core-Shell PtNi/C Alloyed Oxygen Reduction Catalyst. *Int. J. Energy Res.* **2020**, *44* (6), 4773–4783. https://doi.org/10.1002/er.5265.

(35) Beermann, V.; Gocyla, M.; Kühl, S.; Padgett, E.; Schmies, H.; Goerlin, M.; Erini, N.; Shviro, M.; Heggen, M.; Dunin-Borkowski, R. E.; Muller, D. A.; Strasser, P. Tuning the Electrocatalytic Oxygen Reduction Reaction Activity and Stability of Shape-Controlled Pt-Ni Nanoparticles by Thermal Annealing -Elucidating the Surface Atomic Structural and Compositional Changes. *J. Am. Chem. Soc.* **2017**, *139* (46), 16536–16547. https://doi.org/10.1021/jacs.7b06846.

(36) Kühl, S.; Gocyla, M.; Heyen, H.; Selve, S.; Heggen, M.; Dunin-Borkowski, R. E.; Strasser, P. Concave Curvature Facets Benefit Oxygen Electroreduction Catalysis on Octahedral Shaped PtNi Nanocatalysts. *J. Mater. Chem. A* **2019**, *7* (3), 1149–1159. https://doi.org/10.1039/c8ta11298c.

(37) Rudi, S.; Cui, C.; Gan, L.; Strasser, P. Comparative Study of the Electrocatalytically Active Surface Areas (ECSAs) of Pt Alloy Nanoparticles Evaluated by Hupd and CO-Stripping Voltammetry. *Electrocatalysis* **2014**, *5* (4), 408–418. https://doi.org/10.1007/s12678-014-0205-2.

(38) Shviro, M.; Polani, S.; Zitoun, D. Hollow Octahedral and Cuboctahedral Nanocrystals of Ternary Pt-Ni-Au Alloys. *Nanoscale* **2015**, *7* (32), 13521–13529. https://doi.org/10.1039/c5nr03522h.

(39) Polani, S.; Macarthur, K. E.; Klingenhof, M.; Wang, X.; Paciok, P.; Pan, L.; Feng, Q.; Kormányos, A.; Cherevko, S.; Heggen, M.; Korm, A.; Cherevko, S.; Heggen, M.; Strasser, P. Size and Composition Dependence of Oxygen Reduction Reaction Catalytic Activities of Mo-Doped PtNi/C Octahedral Nanocrystals. *ACS Catal.* **2021**, 11407–11415. https://doi.org/10.1021/acscatal.1c01761.

(40) Gan, L.; Rudi, S.; Cui, C.; Heggen, M.; Strasser, P. Size-Controlled Synthesis of Sub-10 Nm PtNi3 Alloy Nanoparticles and Their Unusual Volcano-Shaped Size Effect on ORR Electrocatalysis. *Small* **2016**, 3189–3196. https://doi.org/10.1002/smll.201600027.

(41) Gan, L.; Cui, C.; Heggen, M.; Dionigi, F.; Rudi, S.; Strasser, P. Element-Specific Anisotropic Growth of Shaped Platinum Alloy Nanocrystals. *Science (80-.).* **2014**, *346* (6216), 1502–1506. https://doi.org/10.1126/science.1261212.

(42) Macarthur, K. E.; Slater, T. J. A.; Haigh, S. J.; Ozkaya, D.; Nellist, P. D.; Lozano-Perez, S. Compositional Quantification of PtCo Acid-Leached Fuel Cell Catalysts Using EDX Partial Cross Sections. *Mater. Sci. Technol. (United Kingdom)* **2016**, *32* (3), 248–253. https://doi.org/10.1080/02670836.2015.1133021.

(43) MacArthur, K. E.; Slater, T. J. A.; Haigh, S. J.; Ozkaya, D.; Nellist, P. D.; Lozano-Perez, S. Quantitative Energy-Dispersive X-Ray Analysis of Catalyst Nanoparticles Using a Partial Cross Section Approach. *Microsc. Microanal.* **2016**, *22* (1), 71–81. https://doi.org/10.1017/S1431927615015494.

(44) Peña, F. de la; Prestat, E.; Fauske, V. T.; Burdet, P.; Lähnemann, J.; Furnival, T.; Jokubauskas, P.; Nord, M.; Ostasevicius, T.; MacArthur, K. E.; Johnstone, D. N.; Sarahan, M.; Aarholt, T.; Taillon, J.;

pquinn-dls; Migunov, V.; Eljarrat, A.; Caron, J.; Poon, T.; Mazzucco, S.; Francis, C.; Martineau, B.; actions-user; Somnath, S.; Slater, T.; Tappy, N.; Walls, M.; Cautaerts, N.; Winkler, F.; DENSmerijn. Hyperspy/Hyperspy: Release v1.6.5. **2021**. https://doi.org/10.5281/ZENODO.5608741.

(45) Beermann, V.; Kühl, S.; Strasser, P. Tuning the Catalytic Oxygen Reduction Reaction Performance of Pt-Ni Octahedral Nanoparticles by Acid Treatments and Thermal Annealing. *J. Electrochem. Soc.* **2018**, *165* (15), J3026–J3030. https://doi.org/10.1149/2.0051815jes.

(46) Shviro, M.; Gocyla, M.; Schierholz, R.; Tempel, H.; Kungl, H.; Eichel, R. A.; Dunin-Borkowski, R. E. Transformation of Carbon-Supported Pt-Ni Octahedral Electrocatalysts into Cubes: Toward Stable Electrocatalysis. *Nanoscale* **2018**, *10* (45), 21353–21362. https://doi.org/10.1039/c8nr06008h.

(47) Ahmadi, M.; Behafarid, F.; Cui, C.; Strasser, P.; Cuenya, B. R. Long-Range Segregation Phenomena in Shape-Selected Bimetallic Nanoparticles: Chemical State Effects. *ACS Nano* **2013**, *7* (10), 9195–9204. https://doi.org/10.1021/nn403793a.

(48) Zhao, Z.; Liu, H.; Gao, W.; Xue, W.; Liu, Z.; Huang, J.; Pan, X.; Huang, Y. Surface-Engineered PtNi-O Nanostructure with Record-High Performance for Electrocatalytic Hydrogen Evolution Reaction. *J. Am. Chem. Soc.* **2018**, *140* (29), 9046–9050. https://doi.org/10.1021/jacs.8b04770.

(49) Li, W. X.; Österlund, L.; Vestergaard, E. K.; Vang, R. T.; Matthiesen, J.; Pedersen, T. M.; Lægsgaard, E.; Hammer, B.; Besenbacher, F. Oxidation of Pt(110). *Phys. Rev. Lett.* **2004**, *93* (14), 1–4. https://doi.org/10.1103/PhysRevLett.93.146104.

(50) Urchaga, P.; Baranton, S.; Coutanceau, C.; Jerkiewicz, G. Electro-Oxidation of CO Chem on Pt Nanosurfaces: Solution of the Peak Multiplicity Puzzle. *Langmuir* **2012**, *28* (7), 3658–3663. https://doi.org/10.1021/la202913b.

(51) Van Der Vliet, D. F.; Wang, C.; Li, D.; Paulikas, A. P.; Greeley, J.; Rankin, R. B.; Strmcnik, D.; Tripkovic, D.; Markovic, N. M.; Stamenkovic, V. R. Unique Electrochemical Adsorption Properties of Pt-Skin Surfaces. *Angew. Chemie - Int. Ed.* **2012**, *51* (13), 3139–3142. https://doi.org/10.1002/anie.201107668.

(52) Safo, I. A.; Oezaslan, M. Electrochemical Cleaning of Polyvinylpyrrolidone-Capped Pt Nanocubes for the Oxygen Reduction Reaction. *Electrochim. Acta* **2017**, *241*, 544–552. https://doi.org/10.1016/j.electacta.2017.04.118.

(53) Chunhua Cui, Lin Gan, Marc Heggen, S. R. and P. S. Compositional Segregation in Shaped Pt Alloy Nanoparticles and Their Structural Behaviour during Electrocatalysis. *J. Mater. Chem. A* **2019**, *12* (7), 765–771. https://doi.org/10.1021/acs.nanolett.9b02116.

TOC

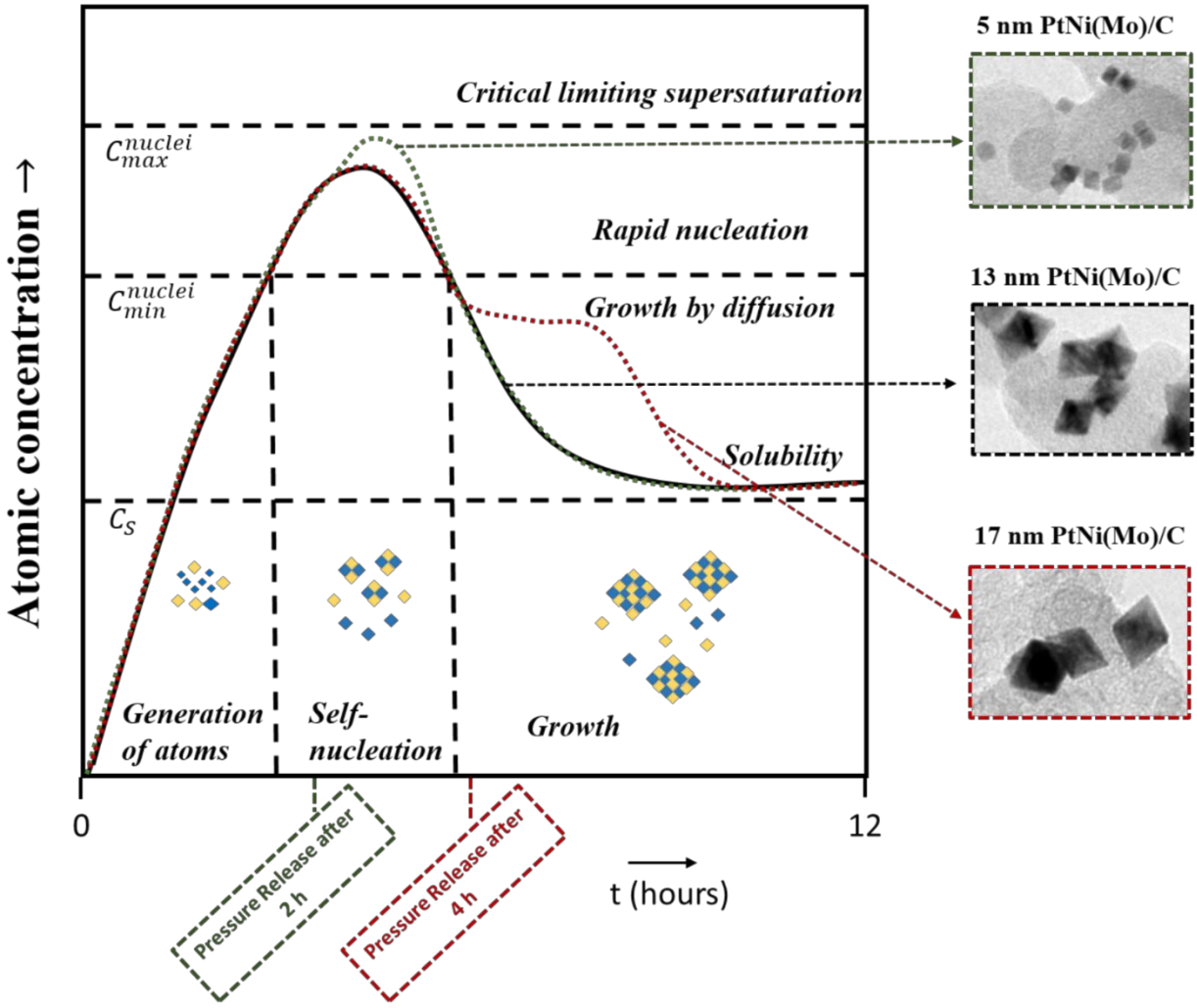
Atomic concentration →
Critical limiting supersaturation
C_{max}^{nuclei}
Rapid nucleation
C_{min}^{nuclei}
Growth by diffusion
Solubility
C_S
Generation of atoms
Self-nucleation
Growth
0
12
t (hours)
Pressure Release after 2 h
Pressure Release after 4 h
5 nm PtNi(Mo)/C
13 nm PtNi(Mo)/C
17 nm PtNi(Mo)/C

Supporting information

Highly Active and Stable Large Mo-doped Pt-Ni Octahedral Catalysts for ORR: Synthesis, Post-treatments and Electrochemical Performance and Stability

Shlomi Polani,[*a†] Katherine E. MacArthur,[b†] Jiaqi Kang,[a] Malte Klingenhof,[a] Xingli Wang,[a] Tim Möller,[a] Raffaele Amitrano,[a] Raphaël Chattot,[c] Marc Heggen,[*b] Rafal E. Dunin-Borkowski,[b] and Peter Strasser[*a]

[a]Electrochemical Energy, Catalysis and Material Science Laboratory, Department of Chemistry, Technical University Berlin, 10623 Berlin, Germany

[b]Ernst-Ruska Centre for Microscopy and Spectroscopy with Electrons and Peter Grünberg Institute, Forschungszentrum Jülich GmbH, 52425 Jülich, Germany

[c]ICGM, Univ. Montpellier, CNRS, ENSCM, 34095 Montpellier cedex 5, France

†These authors contributed equally to the article.

Corresponding Authors

pstrasser@tu-berlin.de
m.heggen@fz-juelich.de
polani@tu-berlin.de

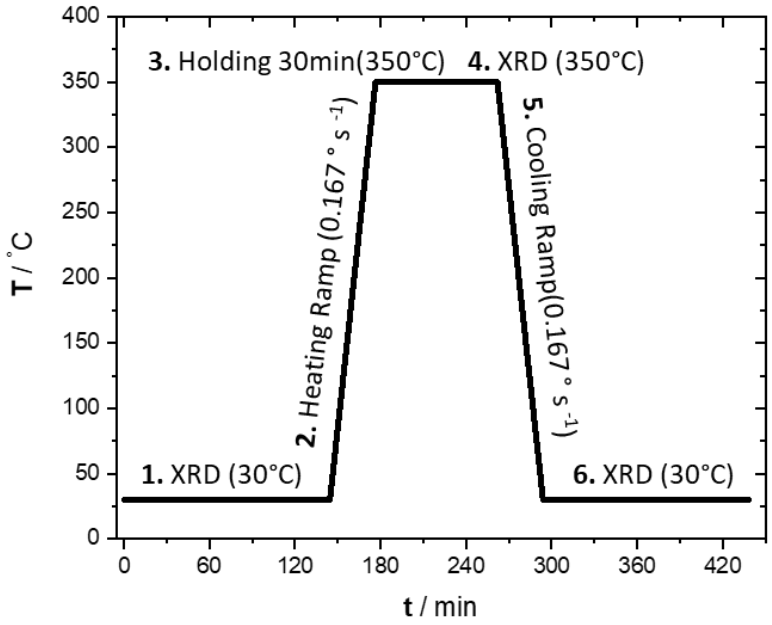

Figure S1. Heating protocol for in situ high-temperature XRD.

Scheme S1. Detailed testing protocols for this study.

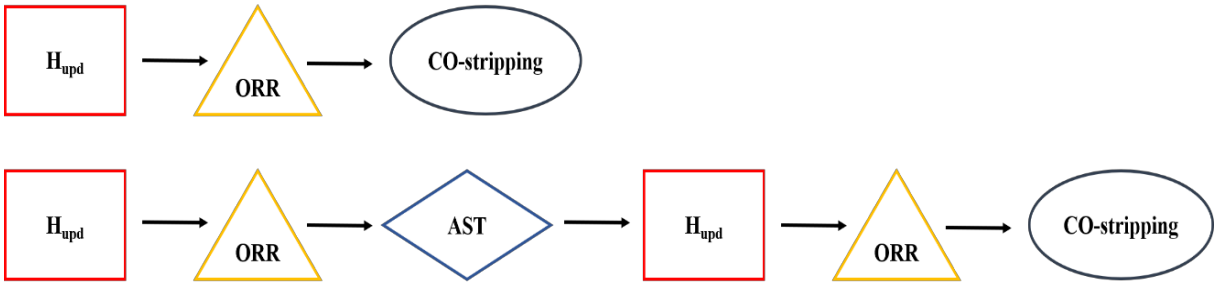

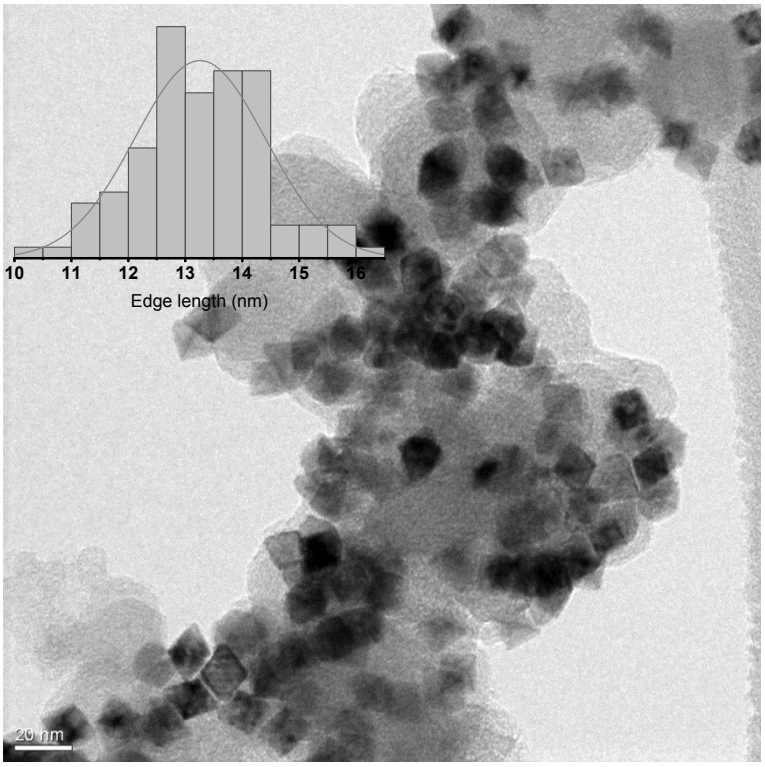

Figure S2. TEM image and the corresponding edge length distribution histogram for PtNi-13 octahedral NPs

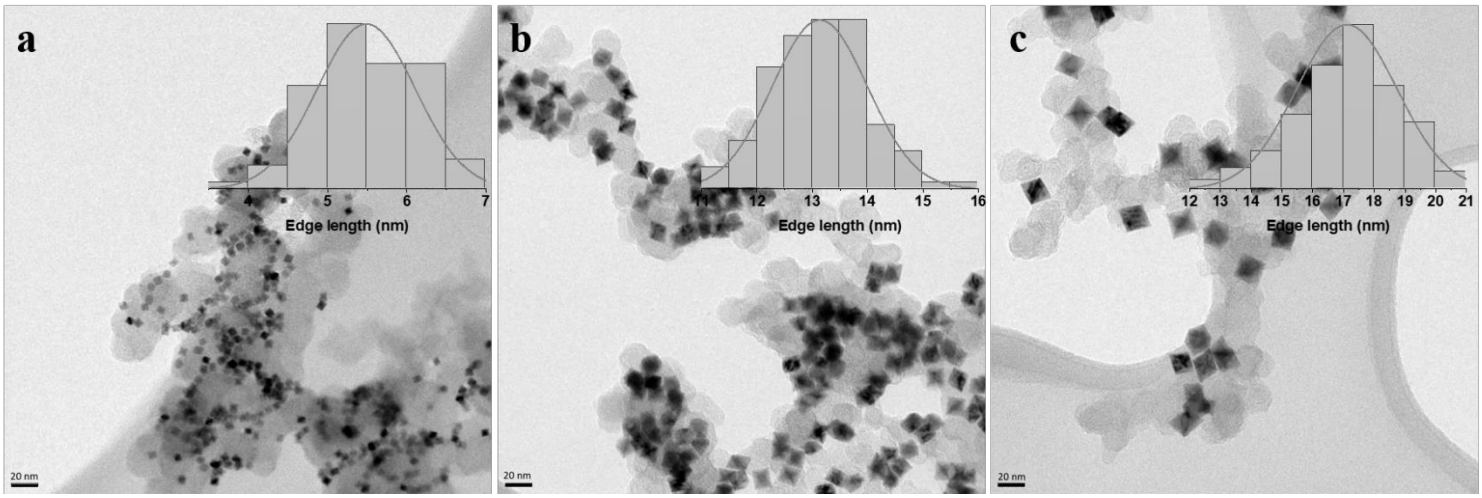

Figure S3. Transmission electron microscopy (TEM) images and the corresponding edge length distribution histogram for PtNi(Mo)/C octahedral NPs (a) PtNi(Mo)-5 (b) PtNi(Mo)-13 (c) PtNi(Mo)-17.

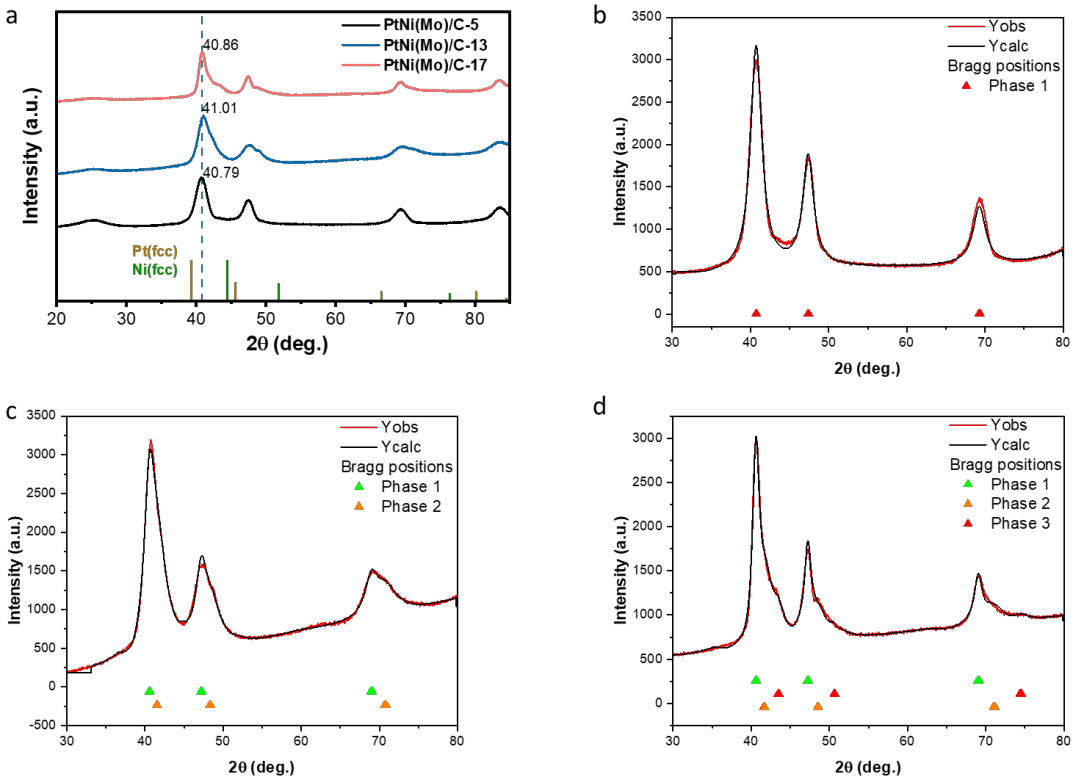

Figure S4. (a) XRD pattern of oh-PtNi(Mo)-5, oh-PtNi(Mo)-13, oh-PtNi(Mo)-17, brown columns correspond to pure Pt (PDF no. 00-004-0802) and green columns to pure Ni (PDF no. 00-004-0850) patterns. The deconvolution of the XRD patterns and the corresponding Bragg positions of the different phases for (b) PtNi(Mo)-5, (c) PtNi(Mo)-13 and (d) PtNi(Mo)-17.

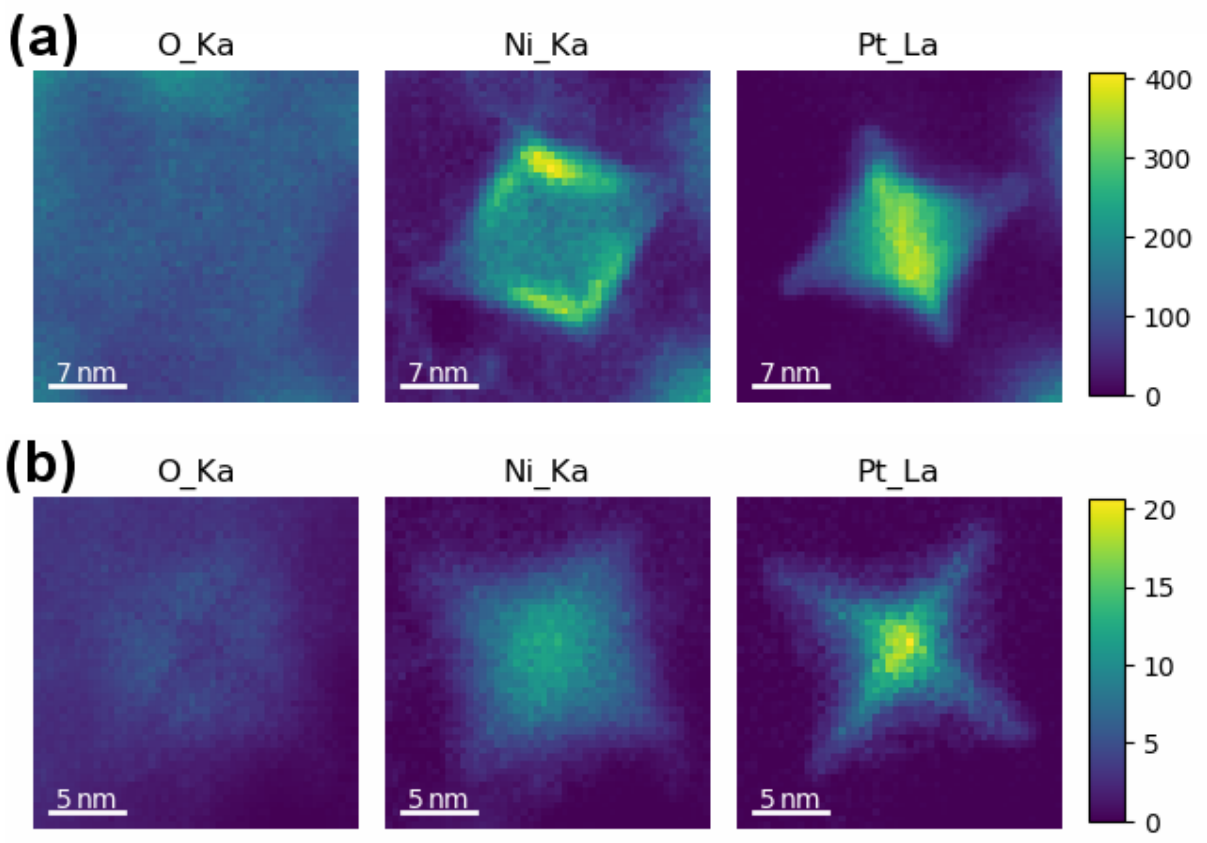

Figure S5. As-prepared oh-PtNi(Mo)-17: EDS Elemental maps, after NMF analysis for O Ka, Ni Ka and Pt La plotted on the same intensity scale viewed (a) along <110> and (b) along <100> directions. The intensity scale is in X-ray counts.

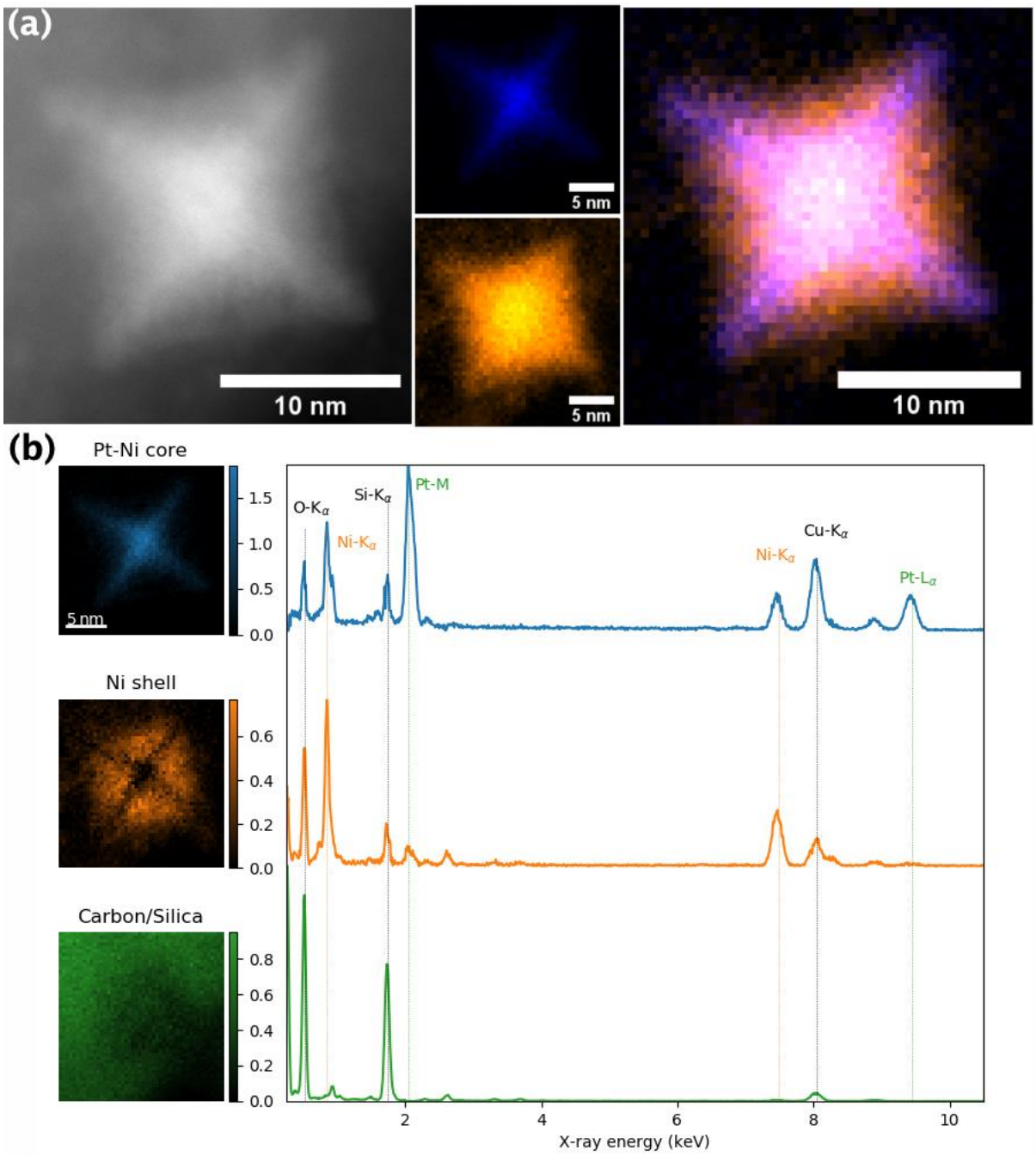

Figure S6. As-prepared oh-PtNi(Mo)-17: (a) ADF-STEM micrographs, STEM-EDS elemental mapping for Pt (blue) and Ni (orange), and their overlay, viewed along a <100> direction. (b) (b) EDS NMF component maps and corresponding spectra show the distribution of a Pt-rich core (blue), a Ni- and O-rich shell (orange), as well as C and Si (green).

Table S1. Metallic at.%, mean edge length, Pt wt% and crystal structure of octahedral PtNi(Mo)/C samples, estimated from ICP-OES, TEM and Rietveld refinement of XRD patterns.

PtNi(Mo)-L	Metallic at% ICP-OES	Mean Edge length (nm)	Pt wt%	Rietveld refinement					
				Phase	Ni at. %	a	wt. %	size [nm]	R_{Bragg} (%)
PtNi(Mo)-5	$Pt_{67.7}Ni_{31}Mo_{1.3}/C$	5.5 ± 0.6	12.6	1	20.843	3.836	100	3.5	1.78
PtNi(Mo)-13	$Pt_{28.2}Ni_{70.8}Mo_{1.0}/C$	13.1 ± 0.9	20.1	1st	17.213	3.851	31.864	3.7	0.54
				2nd	38.338	3.766	68.135	1.9	0.076
PtNi(Mo)-17	$Pt_{32.5}Ni_{67}Mo_{0.5}/C$	17.1 ± 1.6	18.6	1st	18.025	3.847	29.361	6	1.26
				2nd	41.849	3.752	58.255	2.1	0.26
				3rd	78.717	3.605	12.382	3.7	0.32
PtNi(Mo)-17H	$Pt_{31.7}Ni_{67.9}Mo_{0.4}/C$	13.7 ± 1.62	20.4						
PtNi-13	$Pt_{14.7}Ni_{85.3}/C$	13.26 ± 1.15	19.3						

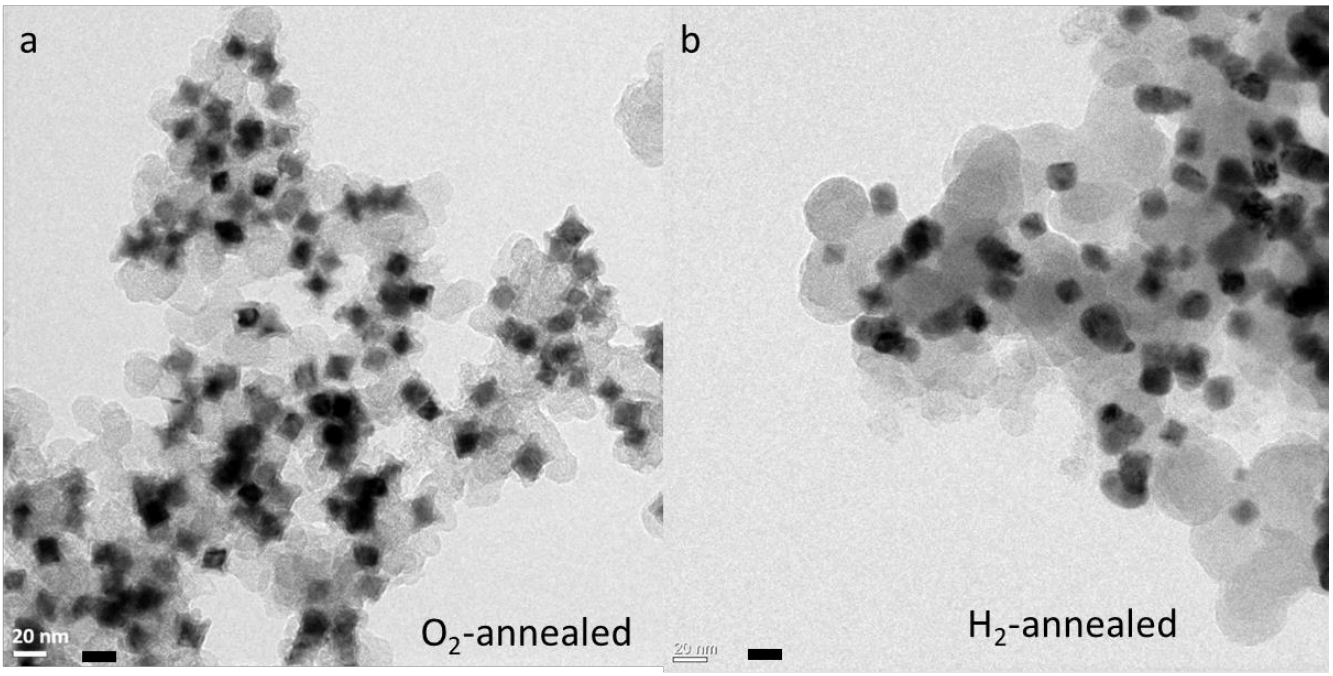

Figure S7. TEM images of oh-PtNi(Mo)-17 after annealing in (a) air or (b) H_2 environment.

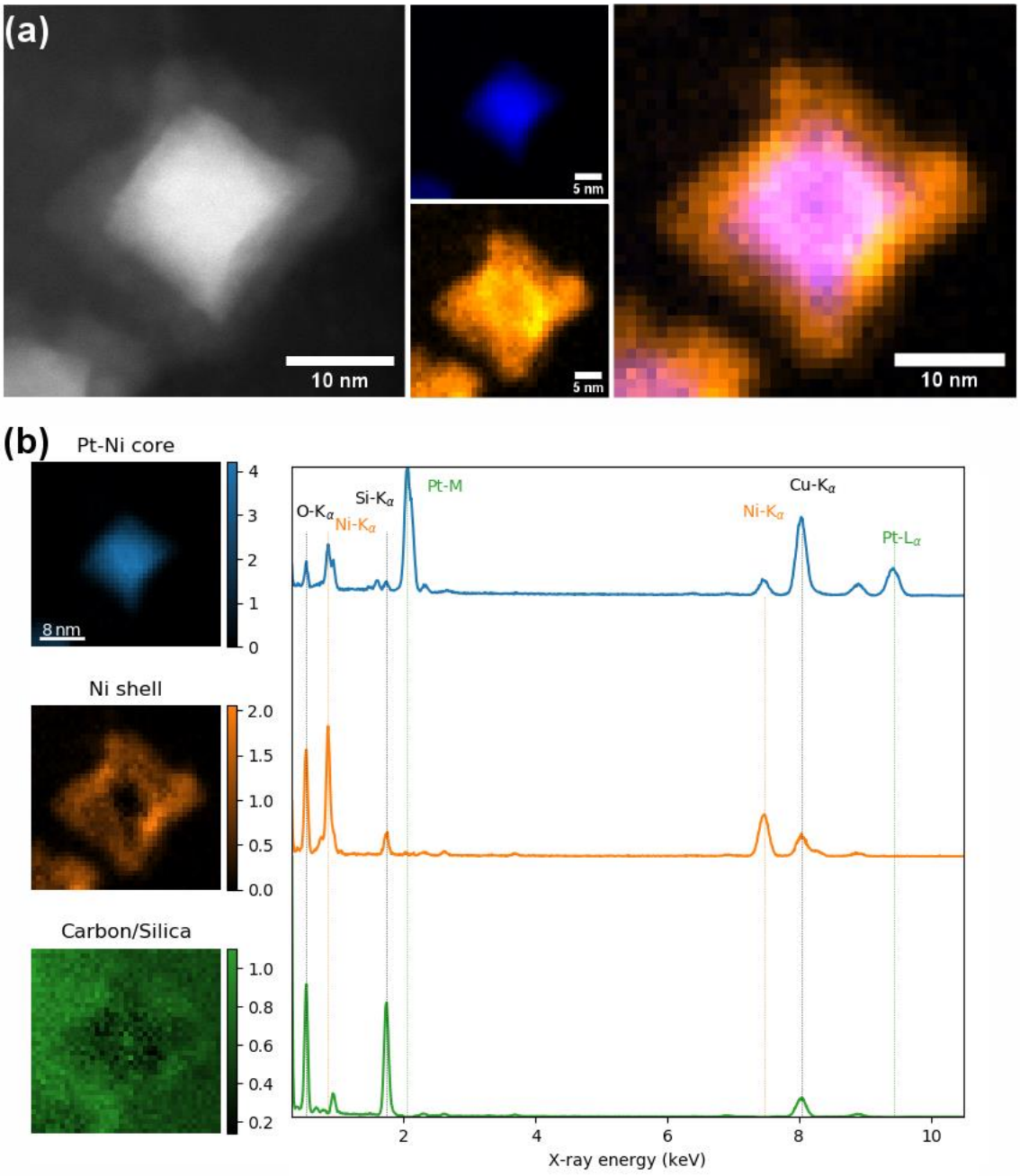

Figure S8. Air-annealed oh-PtNi(Mo)-17A: (a) ADF-STEM micrograph and STEM-EDS elemental mapping for Pt (blue) and Ni (yellow), and their overlay, viewed a) along a <100> direction. (b) EDS NMF component maps and corresponding spectra show the distribution of a Pt-rich core (blue), a Ni- and O-rich shell (orange), as well as C and Si (green).

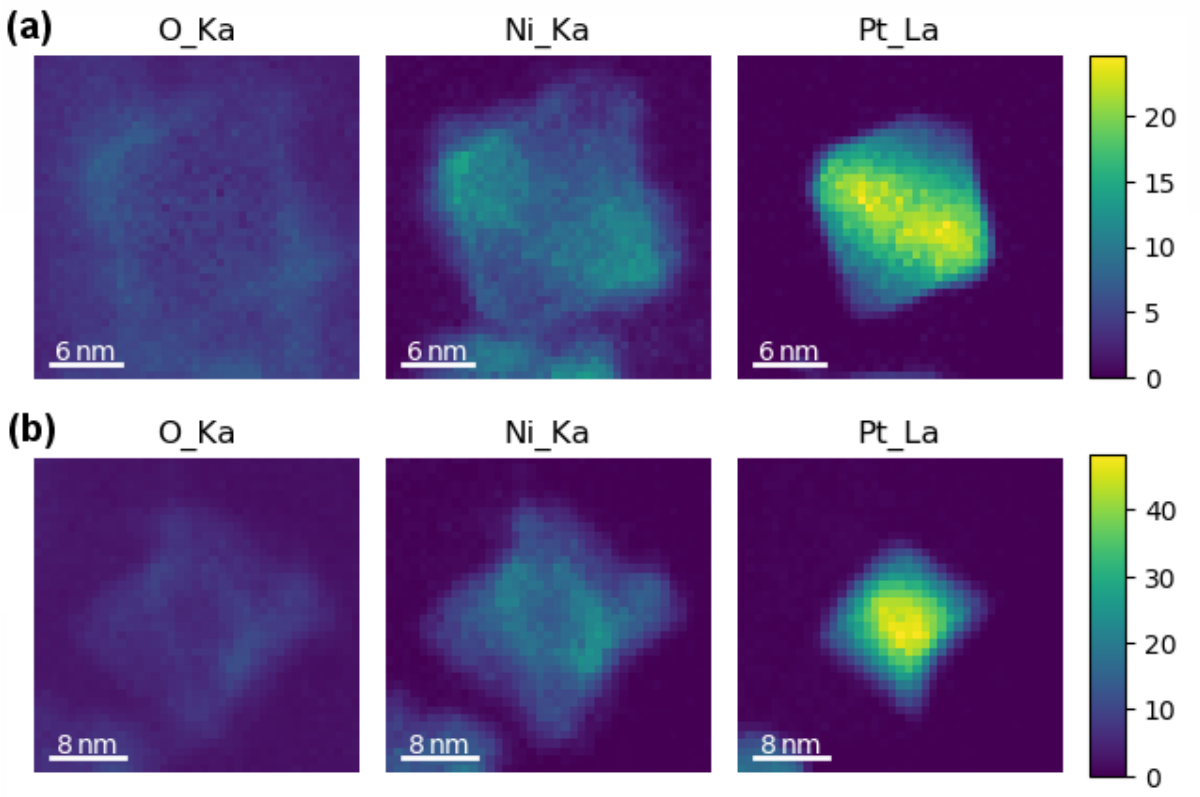

Figure S9. Air-annealed oh-PtNi(Mo)-17A: EDS Elemental maps, after NMF analysis for O Ka, Ni Ka and Pt La plotted on the same intensity scale viewed (a) along <110> and (b) along <100> directions. The intensity scale is in X-ray counts.

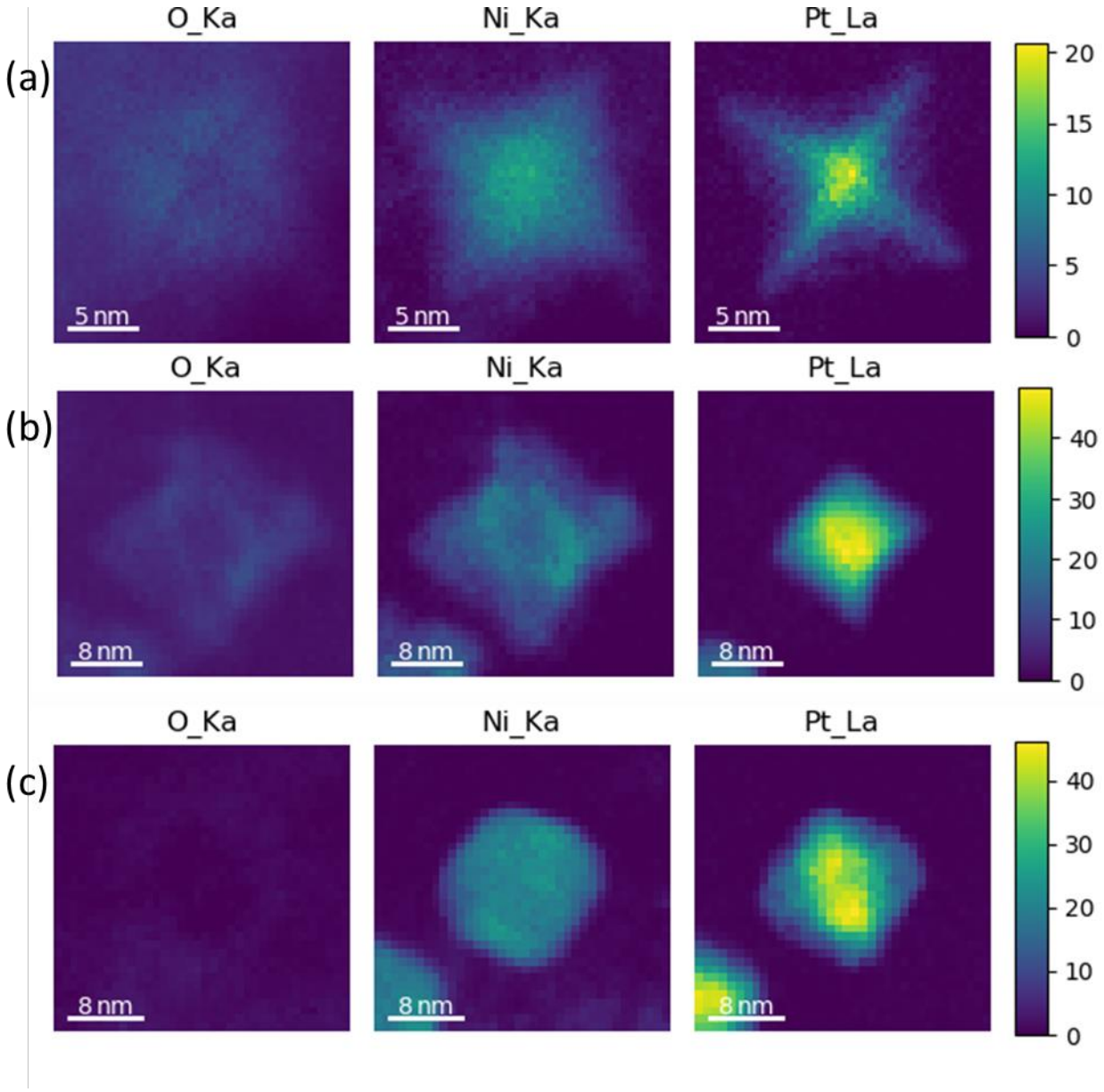

Figure S10. EDS Elemental maps, after NMF analysis for O Ka, Ni Ka and Pt La plotted on the same intensity scale for (a) oh-PtNi(Mo)-17, (b) oh-PtNi(Mo)-17A and (c) oh-PtNi(Mo)-17H structures viewed along the <100> direction. The intensity scale is in X-ray counts.

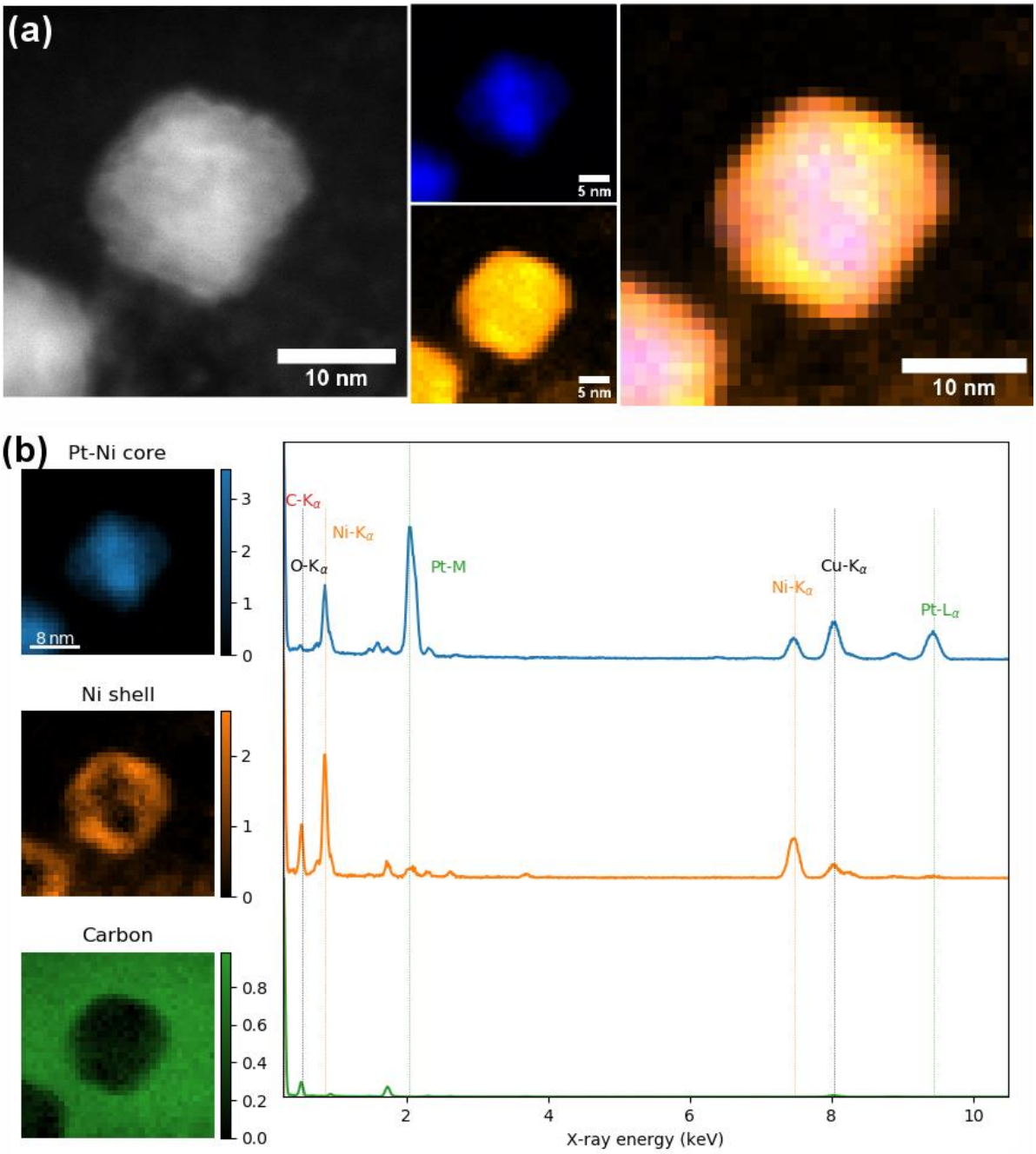

Figure S11. H_2-annealed oh-PtNi(Mo)-17H: (a) ADF-STEM micrograph and STEM-EDS elemental mapping for Pt (blue) and Ni (yellow), and their overlay, viewed a) along a <100> direction. (b) EDS NMF component maps and corresponding spectra show the distribution of a Pt-rich core (blue), a Ni- and O-rich shell (orange), as well as C (green).

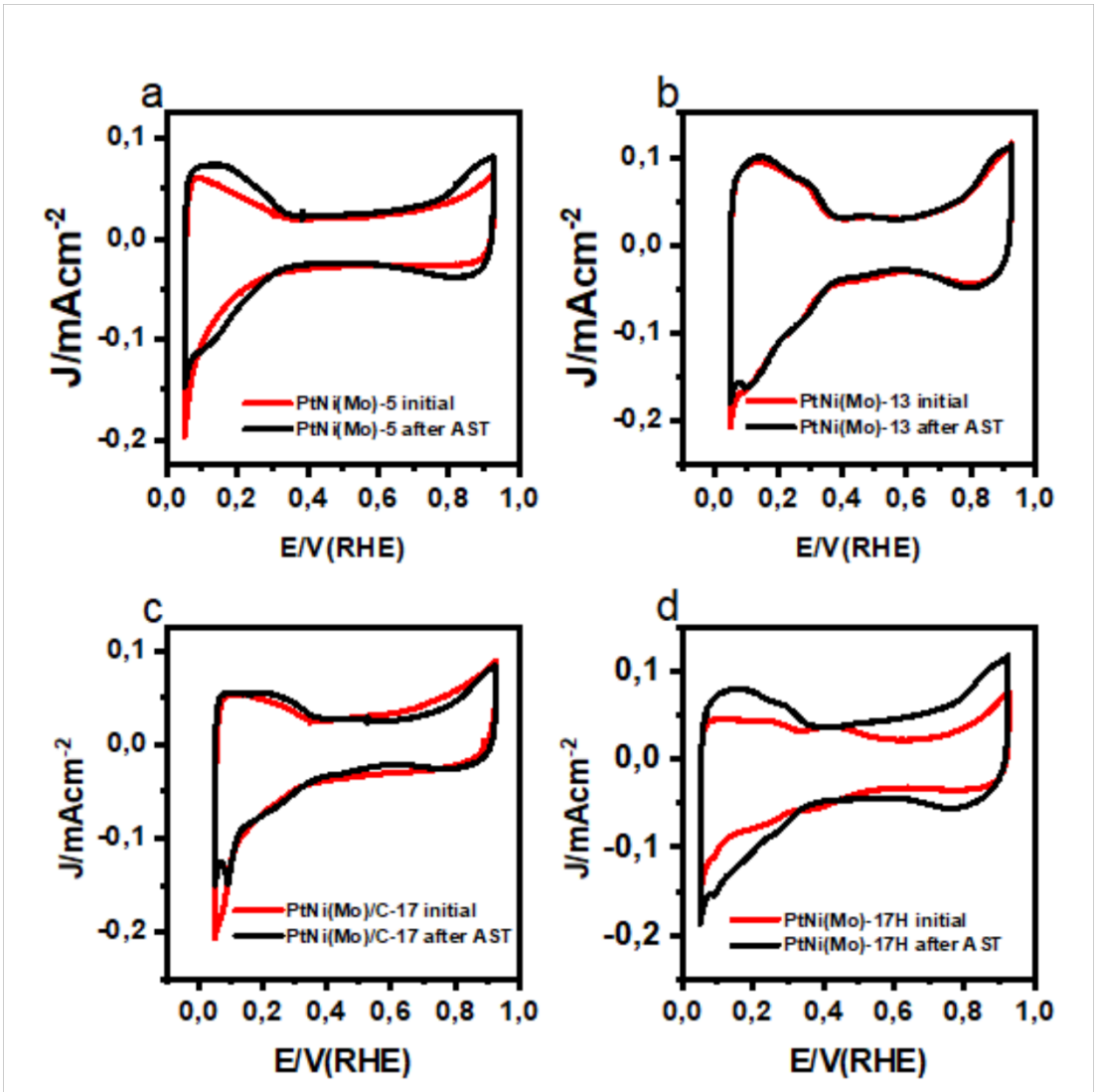

Figure S12. Electrochemical characterization of PtNi(Mo) series (iR corrected): cyclic voltammograms in N_2 saturated linear sweep voltammetry in 0.1M $HClO_4$ electrolyte before (red) and after (black) AST between 0.6–0.95 V_{RHE} for (a) PtNi(Mo)-5, (b) PtNi(Mo)-13, (c) PtNi(Mo)-17 and (d) PtNi(Mo)-17H.

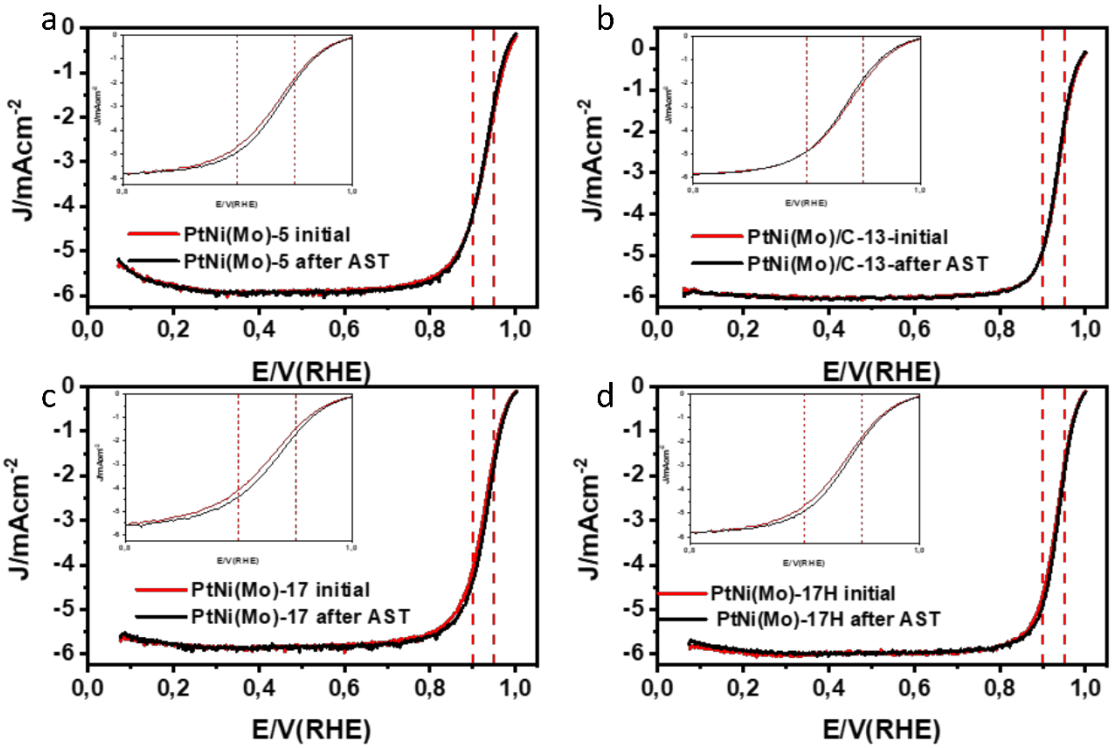

Figure S13. Electrochemical characterization of the PtNi(Mo) series (iR corrected): linear sweep voltammetry in 0.1M $HClO_4$ electrolyte before (red) and after (black) AST between 0.65–0.95 V_{RHE}. Insets show magnification for potentials around 0.9 and 0.95V_{RHE} where activities were sampled, for (a) PtNi(Mo)-5, (b) PtNi(Mo)-13, (c) PtNi(Mo)-17 and (d) PtNi(Mo)-17H.

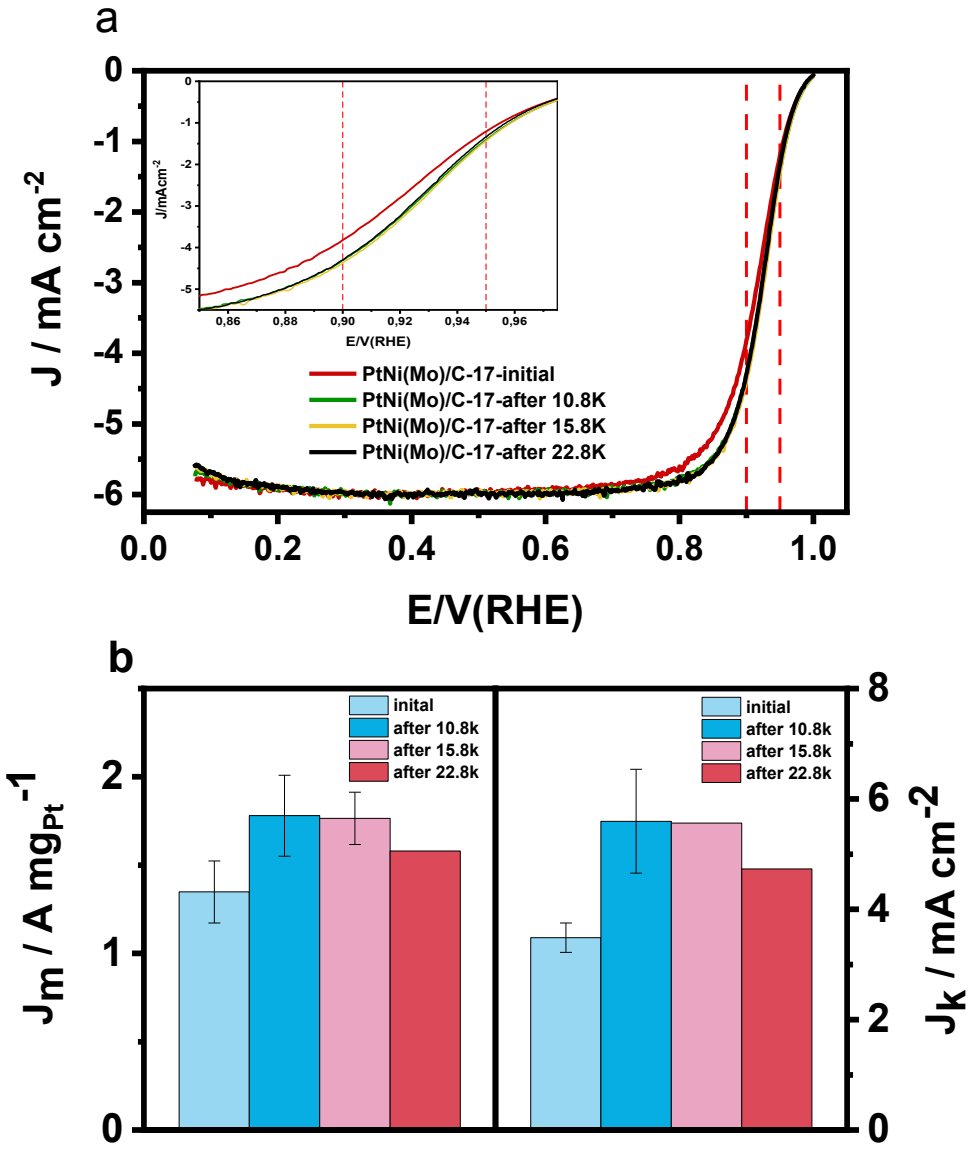

Figure S14. Electrochemical stability testing of PtNi(Mo)-17 (a) ORR polarization curves, inset shows magnification for potentials around 0.9 and 0.95V_{RHE} where activities were sampled (b) Mass activities (left) and specific activities (right).

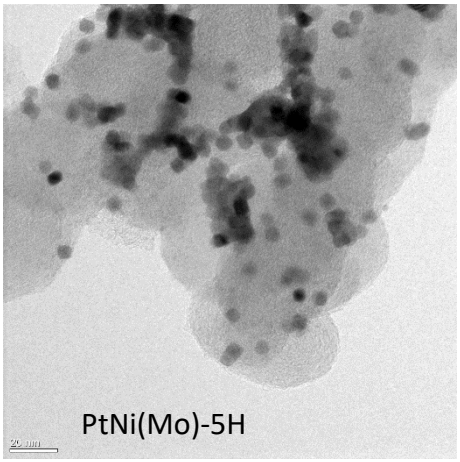

Figure S15. TEM images of (a) oh-PtNi(Mo)-5 after annealing in H_2 environment and (b) as-prepared bimetallic PtNi-13.

Table S2. Electrochemical performance and stability. $ECSA_{Hupd}$ and $ECSA_{CO}$ before and after ASTs, mass and specific activities before and after ASTs (evaluated at 0.9 and 0.95 V_{RHE})

Catalysts	Based on H_{upd} stripping				Based on CO stripping					
	ECSA (m^2/g_{Pt})		Specific activity @0.9 V (@0.95 V) (mA/cm^2)		ECSA (m^2/g_{Pt})		Specific activity @0.9 V (@0.95 V) (mA/cm^2)		Mass activity @0.9 V (@0.95 V) (A/mg_{Pt})	
	Before AST	After AST	Before AST	After AST	Before AST	After AST	Before AST	After AST	Before AST	After AST
PtNi(Mo)-5	43.0	48.4	4.96 (0.89)	4.29 (0.70)	52.3	52.1	4.13 (0.69)	3.98 (0.65)	2.13 (0.37)	2.08 (0.34)
PtNi(Mo)-13	45.3	46.8	5.08 (0.51)	4.80 (0.51)	48.3	46.9	5.14 (0.51)	5.52 (0.55)	2.42 (0.24)	2.26 (0.26)
PtNi(Mo)-17	35.0	36.3	3.76 (0.54)	5.56 (0.74)	39.9	33.8	3.56 (0.50)	5.60 (0.81)	1.40 (0.19)	2.17 (0.27)
PtNi(Mo)-17H	20.8	40.8	10.96 (1.25)	6.55 (0.69)	39.3	38.9	4.88 (0.56)	6.87 (0.73)	2.29 (0.26)	2.65 (0.28)
PtNi(Mo)-5H	26.8	24.1	0.24	0.86	25.0	26.2	0.29	0.79	0.065	0.21
PtNi-13	38.4	41.8	3.71	3.92	32.9	27.9	4.4	5.86	1.45	1.64

References.

(1) Rudi, S.; Cui, C.; Gan, L.; Strasser, P. Comparative Study of the Electrocatalytically Active Surface Areas (ECSAs) of Pt Alloy Nanoparticles Evaluated by Hupd and CO-Stripping Voltammetry. *Electrocatalysis* **2014**, *5* (4), 408–418. https://doi.org/10.1007/s12678-014-0205-2.